JOURNAL OF GEOPHYSICAL RESEARCH, VOL. 104, NO. C8, PAGES 18,205–18,226, AUGUST 15, 1999

Momentum balances on the North Carolina inner shelf

Steve Lentz,[1] R. T. Guza,[2] Steve Elgar,[3] Falk Feddersen,[2] and T. H. C. Herbers[4]

Abstract. Four months of moored current, pressure, temperature, conductivity, wave, and wind observations on the North Carolina shelf indicate three dynamically distinct regions: the surf zone, the inner shelf between the surf zone and the 13-m isobath, and the midshelf. In the surf zone the along-shelf momentum balance is between the cross-shelf gradient of the wave radiation stress and the bottom stress. The linear drag coefficient in the surf zone is about 10 times larger than seaward of the surf zone. On the inner shelf the along-shelf momentum balance is also frictional; the along-shelf wind stress and pressure gradient are balanced by bottom stress. In the cross-shelf momentum balance the pressure gradient is the superposition of roughly equal contributions from the Coriolis force (geostrophy) and wave setdown from shoaling, unbroken surface gravity waves. At midshelf the along-shelf momentum balance is less frictional and hence flow accelerations are important. The cross-shelf momentum balance is predominantly geostrophic because the greater depth and smaller bottom slope at midshelf reduce the importance of wave setdown. The cross-shelf density gradient is in thermal wind balance with the vertical shear in the along-shelf flow in depths as shallow as 10 m. The dominant along-shelf momentum balances provide a simple estimate of the depth-averaged, along-shelf current in terms of the measured forcing (i.e., wind stress, wave radiation stress divergence, and along-shelf pressure gradient) that reproduces accurately the observed cross-shelf variation of the depth-averaged, along-shelf current between the surf zone and midshelf.

1. Introduction

The relative importance of surface gravity wave and wind forcing varies by an order of magnitude between the surf zone (water depths of order 1 m) and the midshelf (water depths of order 100 m). Many observational programs have focused on flows in the surf zone or on the midshelf. However, there are few detailed observational studies of the inner shelf region, between the surf zone and the midshelf, and momentum balances there are understood poorly.

The depth-averaged, along-shelf momentum balance within the surf zone (assuming along-shelf homogeneous bathymetry) is between forcing by obliquely incident breaking surface waves (e.g., gradients in the along-shelf component of the wave radiation stress $\partial S_{xy}/\partial x$), bottom stress, and possibly cross-shelf mixing processes [*Thornton and Guza*, 1986; *Svendsen and Putrevu*, 1994; *Feddersen et al.*, 1998]. (Wave radiation stresses, e.g., S_{xy} and S_{xx}, represent the momentum flux due to surface gravity waves and are analogous to Reynold's stresses [*Longuet-Higgins and Stewart*, 1964]. Unless noted otherwise, the timescales of interest are a few days, long compared with surface wave periods, and variables are averages over many wave periods). Recent studies [*Whitford and Thornton*, 1993; *Feddersen et al.*, 1998] suggest the along-shelf wind stress is sometimes significant in the surf zone but is usually much smaller than $\partial S_{xy}/\partial x$. The along-shelf momentum balance at midshelf is complex. Acceleration, Coriolis force, pressure gradients, wind stress, and bottom stress are each important on various shelves [*Allen and Smith*, 1981; *Lentz and Winant*, 1986; *Lee et al.*, 1984, 1989]. Previous studies indicate the inner shelf is dynamically different with along-shelf flows driven by both along-shelf wind stress and along-shelf pressure gradients, and these forcing terms are balanced primarily by bottom friction [*Scott and Csanady*, 1976; *Pettigrew*, 1981; *Lentz and Winant*, 1986; *Masse*, 1988; *Lee et al.*, 1989; *Lentz*, 1994].

The depth-averaged, cross-shelf momentum balance within the surf zone is between gradients of the cross-shelf radiation stress ($\partial S_{xx}/\partial x$) associated with wave breaking and the cross-shelf pressure gradient $\partial P/\partial x$ (i.e., wave setup) [*Longuet-Higgins and Stewart*, 1964; *Bowen et al.*, 1968; S. J. Lentz and B. Raubenheimer, Field observations of wave setup, submitted to *J. Geophys. Res.*, 1998] (hereinafter referred to as submitted manuscript 1998). The cross-shelf momentum balance over the midshelf is between $\partial P/\partial x$ and the Coriolis force associated with the along-shelf flow (i.e., geostrophic) [*Brown et al.*, 1985, 1987; *Lee et al.*, 1989]. As the depth decreases setup (or setdown) forced by the cross-shelf wind stress will become increasingly important. On the South Carolina shelf in 10 m of water, $\partial P/\partial x$, the Coriolis force, and the cross-shelf wind stress were estimated to be approximately equal in magnitude [*Lee et al.*, 1989]. However, $\partial P/\partial x$ was estimated as the difference between two pressure sensors spanning the entire 75-km-wide shelf. Furthermore, surface waves were not measured and thus the wave setdown associated with $\partial S_{xx}/\partial x$ in unbroken shoaling waves [*Bowen et al.*, 1968] could not be estimated. The relative importance of surface wave forcing, Coriolis force, and cross-shelf wind stress in the cross-shelf momentum balance over the inner shelf is unknown.

Previous studies have generally included, at most, one moor-

[1]Woods Hole Oceanographic Institution, Woods Hole, Massachusetts.
[2]Center for Coastal Studies, Scripps Institution of Oceanography, University of California, San Diego, La Jolla.
[3]School of Electrical Engineering and Computer Science, Washington State University, Pullman.
[4]Department of Oceanography, Naval Postgraduate School, Monterey, California.

Paper number 1999JC900101.
0148-0227/99/1999JC900101$09.00

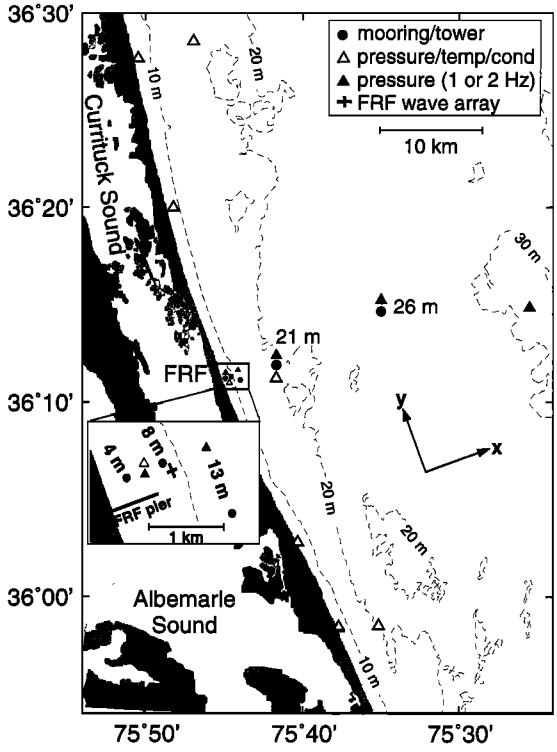

Figure 1. Plan view of the study region and instrument locations. The central cross-shelf transect of instruments is shown in detail in Figure 2.

ing site between the 5- and 30-m isobaths, so that little is known about the momentum balances across the inner shelf. More detailed observations across the inner 16 km of the North Carolina shelf are used here to determine the cross-shelf variation of the dominant terms in the depth-averaged cross- and along-shelf momentum balances. The observations, in water depths ranging from 4 to 26 m, span the region from the surf zone to midshelf and include simultaneous measurements of currents, winds, waves, and pressures. An overview of the observations is given in section 2. Momentum balances are described in section 3. Simplified scalings of the observed dominant balances are considered in section 4, followed by a summary in section 5.

2. Background

2.1. Field Program and Data Processing

Observations were obtained offshore of the Army Corps of Engineers' Field Research Facility (FRF) on the Outer Banks near Duck, North Carolina, from August through early December 1994 as part of the interdisciplinary Coastal Ocean Processes Inner Shelf Study [*Butman*, 1994]. The site is about midway between Cape Henry, at the mouth of Chesapeake Bay (100 km to the north), and Cape Hatteras. The coastline is relatively straight between Cape Henry and Oregon Inlet (50 km to the south), with an orientation of about 340°T at the array center (Figure 1). The bathymetry inshore of the 20-m isobath is approximately homogeneous along shelf on scales of many kilometers. Offshore of the 20-m isobath the complex ridge and swale bathymetry varies several meters vertically over horizontal scales of a few kilometers (Figure 2). The seafloor slopes relatively steeply (0.01) from the 4-m to the 13-m isobath and more gently (0.002) from the 13-m to the 20-m isobath. Offshore of the 20-m isobath the seafloor slope is small (0.0002) over cross-shelf scales large compared with the ridge and swale features.

Two rigid towers (in 4- and 8-m water depth) and three surface/subsurface mooring pairs (in 13-, 21-, and 26-m water depth) were deployed along a 16-km cross-shelf transect (Figure 2). The towers supported Marsh-McBirney electromagnetic current meters and fast-response thermistors sampled at 2 Hz, with vertical spacings of about 1 m or less. The moorings supported vector-measuring current meters that measure horizontal currents and temperature and Sea-Bird Seacats that measure temperature and conductivity, all with sample rates of 4 min. Vertical separations for these instruments were 1 to 5 m (Figure 2). Two Seacats were also deployed 1 and 4 m above the bottom on a piling of the FRF pier in about 8-m depth. Setra pressure sensors, sampled at 1 or 2 Hz to measure surface gravity waves, were deployed about 1 m above the seafloor near each mooring or tower and also in 33-m depth (about 30-km offshore, Figure 2). The FRF maintains a wave-directional array of 15 pressure sensors in 8-m depth extending about 200 m along shelf and 60 m cross shelf and sampled at 2 Hz [*Long*, 1996]. Wind velocity was measured 3.5 m above the sea surface at the 21-m site (sample rate 7.5 min) and 19.5 m above the sea surface on the FRF pier.

Along-shelf pressure gradients were estimated from an array of eight Sea-Bird Seagauges that each measure pressure, temperature, and conductivity. The Seagauges were deployed about 1 m above the bottom, with five along the 5-m isobath and three along the 21-m isobath, in both cases spanning an along-shelf distance of about 60 km (Figure 1). Additionally, at the northern and southern 21-m sites, Seacats were mounted 1 m below the sea surface on surface buoys. Along-shelf array instruments were sampled every 4 min. Bottom pressure was averaged over the 4-min sample interval. Cross-shelf pressure gradients on the array center line were estimated using the Seagauges on the 5-m and 21-m isobaths, and the 1- or 2-Hz

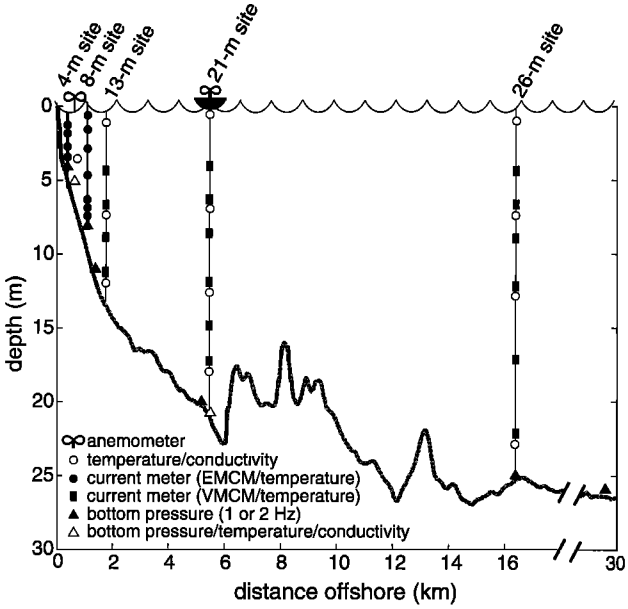

Figure 2. Cross-shelf instrument transect along the central line. Thick curve is the bathymetry (depth relative to mean sea level).

sampling Setra pressure gauges on the 11-m, 26-m, and 33-m isobaths (section A1).

The instrumentation was deployed during late July and early August and recovered either at the end of October or in early December 1994. The 8-m tower and the 13-m surface mooring both failed about October 10, during a strong nor'easter. The 21-m surface mooring failed during a nor'easter on September 4, came ashore, was refurbished, and redeployed on October 4. Both the 21- and 26-m surface moorings failed during Hurricane Gordon (November 16) and came ashore. The instrumentation and data were recovered after these failures. Time series from the 4- and 8-m sites have gaps owing to maintenance, intermittent problems with individual instruments, and a severe lightning strike in early August.

All time series (with the exception of surface wave data) were block averaged to hourly values centered on the hour. The focus is on subtidal dynamics, so time series were low-pass filtered (half-power point 38 hours) unless noted otherwise. All vector time series were rotated to a coordinate system based on the coastline orientation (Figure 1), with the along-shelf coordinate y positive toward 340°T and the cross-shelf coordinate x positive offshore. Obvious biases and drifts in some conductivity time series were identified and corrected by comparisons with adjacent moored conductivity cells and shipboard conductivity-temperature-depth (CTD) data obtained near the moorings [*Alessi et al.*, 1996; *Waldorf et al.*, 1995, 1996]. Data were discarded from near-bottom conductivity cells that drifted substantially in late October, presumably because of fouling by suspended sediment. Salinity and density were estimated using the temperature and corrected conductivity [*Fofonoff and Millard*, 1983]. Pressure time series from sensors mounted on anchors (water depths greater than 8 m) sometimes show positive shifts of 1–30 mbar during storms, presumably owing to scouring and settling of the anchors. Anchor shifts greater than 1 mbar were identified and removed by comparison with time series from other near-bottom pressure sensors (rigidly mounted on jetted pipes in shallower water) that did not shift. A more detailed description of data return and initial processing, including correction of conductivity time series and removal of anchor shifts from pressure time series, is given by *Alessi et al.* [1996].

2.2. Overview of Observations

The dominant timescale of wind variability is a few days, associated primarily with the passage of cold fronts [*Austin and Lentz*, this issue]. Comparison of winds from the FRF pier (8-m depth), the 21-m site, and several National Data Buoy Center (NDBC) buoys in the region indicate that subtidal winds did not vary substantially across the 16-km cross-shelf extent of the study region during the field program (section A2). Wind directions are typically 45° to the coast, either poleward (upwelling favorable) and offshore or equatorward (downwelling favorable) and onshore. The strongest wind stresses (section A1) were associated with nor'easters (downwelling favorable) (Figure 3). Significant wave heights H_{sig} at the 8-m wave array ranged from 0.2 to 4 m (Figure 3) and are correlated with the wind stress magnitude. Hourly averaged wave directions at the array ranged between +50° and −50° from normally incident, i.e., wave crests parallel to the coast.

Along-shelf current variance over timescales from hours to weeks is dominated by subtidal variability. At all five sites the correlation between subtidal along-shelf currents at different levels in the water column is greater than 0.75 (the 95% confidence level for a correlation significantly different from zero is 0.45, assuming a decorrelation timescale of 3 days and 60-day-long time series). Subtidal along-shelf currents tend to decrease by roughly a factor of 3 from near the surface to near the bottom. The much weaker subtidal cross-shelf currents u are not well correlated over the water column at any site and are often in opposite directions near the surface and bottom. Depth-averaged and subtidal (e.g., low-pass filtered, section A1) currents are considered here unless otherwise noted.

The mean, depth-averaged, along-shelf flow $\bar{v}$ is equatorward at all five sites, 9 cm s^{-1} at the 13-m site and 4–5 cm s^{-1} at the 4- and 26-m sites (Table 1). Although the data do not span the same time period (Figure 3), the cross-shelf structure for a shorter common time period is similar.

The principal axes of the depth-averaged currents are along shelf to the accuracy of the measurements (≈5°) with standard deviations of 13–20 cm s^{-1} (Table 1). Correlations between depth-averaged, along-shelf currents measured at the five cross-shelf sites range from 0.64 to 0.94. In contrast to the depth-averaged, along-shelf flow, both the means and standard deviations of the depth-averaged cross-shelf flow $\bar{u}$ are small relative to the accuracy of the current measurements (2–3 cm s^{-1}) [*Beardsley*, 1987; *Guza et al.*, 1988]. Depth-averaged, cross-shelf currents at different moorings are generally not correlated, consistent with error-dominated measurements and/or unresolved spatial variation of the current. In either case, estimates of terms in the momentum balances associated with $\bar{u}$ must be interpreted cautiously. Though a few centimeters per second or less, $\bar{u}$ may still be important for cross-shelf exchange because the inner shelf region is so narrow.

The vertical structure of temperature evolved dramatically during the study (Figure 4a). In August, 23°C near-surface water and deeper 17°C water were separated by a strong thermocline centered about 10 m below the surface. Wind-driven upwelling (downwelling) of the thermocline in August resulted in large cross-shelf temperature gradients onshore of the 26-m site as the thermocline shoaled (deepened) and formed a surface (bottom) front. The water column was vertically mixed at least as far offshore as the 26-m site in response to strong winds from the northeast in early September. A strong thermocline did not redevelop and temperature differences across the water column often were much less than 2°C from September through November.

Despite the strong thermocline in August, both vertical (Figure 4) and cross-shelf density gradients were dominated by salinity variations. The primary source of salinity variability was narrow, shallow plumes of relatively fresh water, presumably from Chesapeake Bay [*Rennie et al.*, this issue]. The Chesapeake Bay plume flowed into the study region generally during downwelling-favorable winds and was typically confined inshore of the 21-m isobath until it was swept offshore by upwelling-favorable winds. When the Chesapeake Bay plume was not present, salinities generally increased with depth and distance offshore, consistent with historical data [*Boicourt*, 1973]. Vertical salinity (and hence density) gradients tended to be large during August and small during October when there was strong wind and wave forcing (Figure 3).

3. Momentum Balances

The depth-averaged momentum equations, assuming hydrostatic flow and small sea level variations compared with the water depth, are

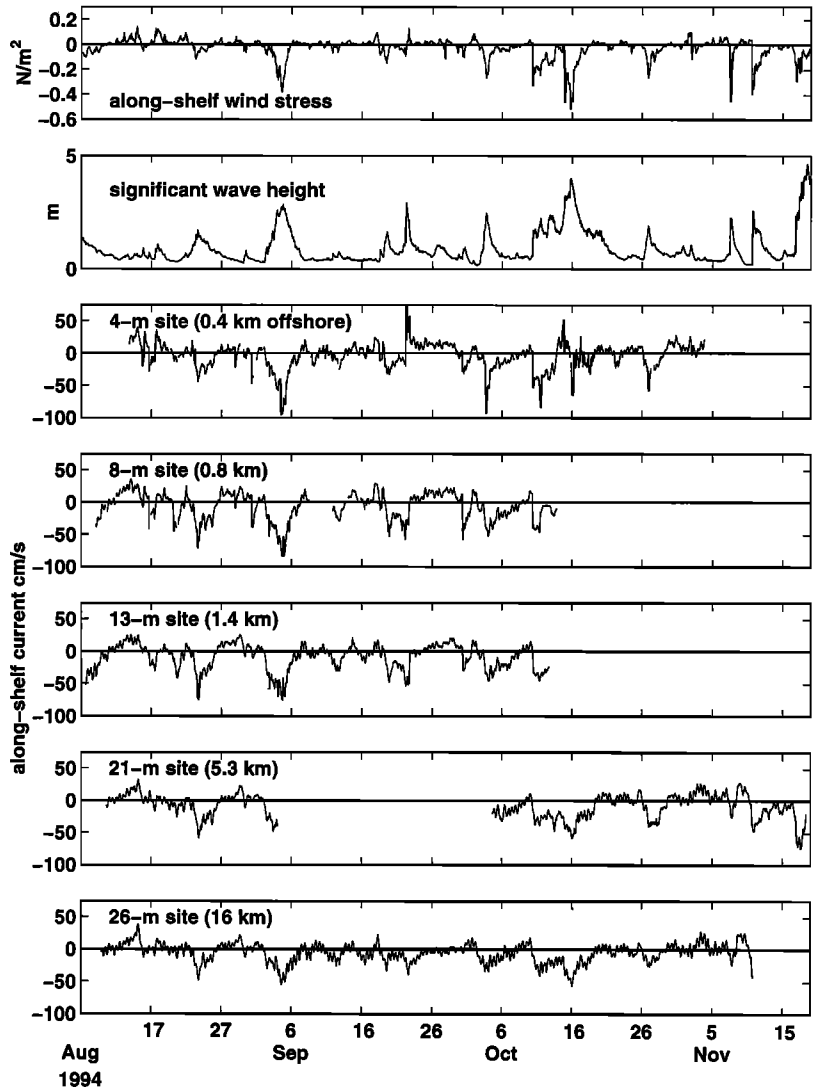

Figure 3. Time series of the along-shelf wind stress (negative is equatorward); significant wave height in 8-m water depth; and the subtidal depth-averaged, along-shelf current at the five mooring sites. Offshore distances of mooring sites are in parentheses.

$$\frac{\partial \bar{u}}{\partial t} + \frac{1}{h}\frac{\partial}{\partial x}\int_{-h}^{0} u^2\,dz + \frac{1}{h}\frac{\partial}{\partial y}\int_{-h}^{0} uv\,dz - f\bar{v} = -\frac{1}{\rho_0}\frac{\partial P}{\partial x} + \frac{\tau^{sx}}{\rho_0 h} - \frac{\tau^{bx}}{\rho_0 h} - \frac{1}{\rho_0 h}\frac{\partial S_{xx}}{\partial x} \quad (1)$$

$$\frac{\partial \bar{v}}{\partial t} + \frac{1}{h}\frac{\partial}{\partial x}\int_{-h}^{0} uv\,dz + \frac{1}{h}\frac{\partial}{\partial y}\int_{-h}^{0} v^2\,dz + f\bar{u} = -\frac{1}{\rho_0}\frac{\partial P}{\partial y} + \frac{\tau^{sy}}{\rho_0 h} - \frac{\tau^{by}}{\rho_0 h} - \frac{1}{\rho_0 h}\frac{\partial S_{xy}}{\partial x} \quad (2)$$

Table 1. Statistics of Depth-Averaged Currents

	Mean		Principal Axes			
Site	$\bar{u}$	$\bar{v}$	Major	Minor	Orientation, deg	Days
4 m	2	−4	18	6	4	79
8 m	1	−7	20	2	−1	61
13 m	−1	−9	19	2	−4	66
21 m	−1	−8	18	2	−3	69
26 m	−2	−5	13	2	2	93

Values of cross-shelf $\bar{u}$ and along-shelf flow $\bar{v}$ are in centimeters per second. Orientations are relative to the along-shelf direction 340°T. Time series span different time periods (see Figure 3).

where (u, v) are the cross-shelf (x) and along-shelf (y) subtidal components of velocity, $(\bar{u}, \bar{v})$ are the corresponding depth-averaged velocities, z is height above mean sea level, h is the water depth, $f = 8.59 \times 10^{-5}$ s^{-1} is the Coriolis parameter, $\rho_0 = 1023$ kg m^{-3} is a reference density, $(\partial P/\partial x, \partial P/\partial y)$ is the depth-averaged horizontal pressure gradient, $g = 9.81$ m s^{-2} is gravitational acceleration, (τ^{sx}, τ^{sy}) is the wind stress, (τ^{bx}, τ^{by}) is the bottom stress, and S_{xx} and S_{xy} are wave radiation stresses. Lateral mixing processes on timescales shorter than subtidal may be significant, especially in the surf zone, but are not included because they could not be estimated accurately from the observations. Along-shelf gradients in the surf zone radiation stress and pressure fields at relatively short

spatial scales (e.g., associated with local along-shelf bathymetric variations) could not be estimated. Support for neglecting along-shelf variations in the along-shelf momentum balance (2) inshore of the 8-m isobath is provided by *Feddersen et al.* [1998].

The depth-averaged pressure gradient (obtained by vertically integrating the hydrostatic equation) includes surface pressure P^s and density ρ contributions

$$\frac{\partial P}{\partial x} = \frac{\partial P^s}{\partial x} + \int_{-h}^{0} g \frac{\partial \rho}{\partial x}\left(1 + \frac{z}{h}\right) dz \qquad (3)$$

with a corresponding equation for $\partial P/\partial y$. Here $\partial P^s/\partial x$ includes contributions from the sea surface slope and the atmospheric pressure gradient and will be referred to as the barotropic pressure gradient. The second term on the right-hand side of (3), the density contribution to the depth-averaged pressure gradient, will be referred to as the baroclinic pressure gradient. Assuming hydrostatic flow, the near-surface pressure in (3) may be expressed in terms of near-bottom pressure P^b and density

$$P^s = P^b - \int_{-h}^{0} \rho g \, dz. \qquad (4)$$

The terms in (1)–(3) are estimated at some or all of the five mooring sites. Cross-shelf gradients are estimated as finite differences centered on the mooring sites. An alternate approach, estimating terms in control volumes bounded by adjacent moorings, yields similar results. The nonlinear terms on the left-hand side of (1) and (2) could not be estimated accurately at the 4- and 8-m sites because the wave height can be a significant fraction of the water depth and the water column above the wave trough level (where u is onshore) was not sampled. Crude estimates suggest the nonlinear terms at the deeper sites were small. The nonlinear terms are not considered further. Estimation of the other terms is described in section A1, and uncertainties in some estimates are discussed in section A2. Bottom stress is estimated using a linear drag law

$$(\tau^{bx}, \tau^{by}) = \rho_0 r (u_b, v_b) \qquad (5)$$

where $r = 5 \times 10^{-4}$ m s^{-1} based on previous midshelf observations [e.g., *Lentz and Winant*, 1986] and (u_b, v_b) is the velocity 0.5 to 1.5 m above the bottom. Bottom stress estimates from (5) are similar to log-profile estimates using bottom tripod measurements at the 21-m site (Section A3), suggesting a constant r provides reasonable bottom stress estimates at this site. However, the along-shelf momentum balance discussed in section 3.1 implies r is substantially larger in the surf zone.

The time average over the deployment period of terms in the cross- and along-shelf momentum balances either could not be estimated (e.g., mean pressure gradients) or are small compared with the fluctuations in those terms and are not considered further.

3.1. Along-Shelf Momentum Balance

At the 4-m site, time series of the along-shelf wind (τ^{sy}) and bottom stresses (τ^{by} from (5)) are similar (Figure 5a). Exceptions occur during portions of October 14–15 and September 22, when the along-shelf wind and along-shelf current are opposed (e.g., τ^{sy} and τ^{by} have opposite signs in Figures 5a and 8a, discussed below). At these times the wave radiation stress gradient opposed the wind stress, the 4-m site was in the surf zone, and the 4-m along-shelf current was in the direction of the wave radiation stress gradient, indicating the dominant driving force was the radiation stress gradient $\partial S_{xy}/\partial x$ resulting from obliquely incident breaking waves (Figure 5b). To examine where wind or waves dominate the along-shelf forcing, it is convenient to categorize each site (for each hourly time period) as either seaward of, or in, the surf zone, even though the demarcation between the surf zone and the inner shelf is not sharp. For simplicity, a site is considered seaward of the surf zone if $H_{sig}/h < 0.33$, corresponding to breaking of less than about 10% of the waves [*Thornton and Guza*, 1984]. Surface wave heights at each site were estimated using a nearby bottom pressure gauge and linear theory. Using this criterion, the 4-m site was in the surf zone on August 23, September 3–6, 19, and 22, and October 3–4 and 10–20. The 4-m site is within the surf zone when $\partial S_{xy}/\partial x$ is large (Figure 5b) and also when H_{sig} is large, but the wave direction is close to normally incident so $\partial S_{xy}/\partial x$ (see (A3)) is small. The 8-m tower was in the surf zone for a few hours on September 4 and 22. The 21- and 26-m sites were never in the surf zone, and the 8-m tower and 13-m surface mooring failed during the large waves in mid-October. More complicated expressions for defining the offshore extent of the surf zone [e.g., *Battjes and Stive*, 1985] yield similar estimates, and the results below do not depend critically on this definition.

When the 4-m site is in the surf zone, the standard deviation

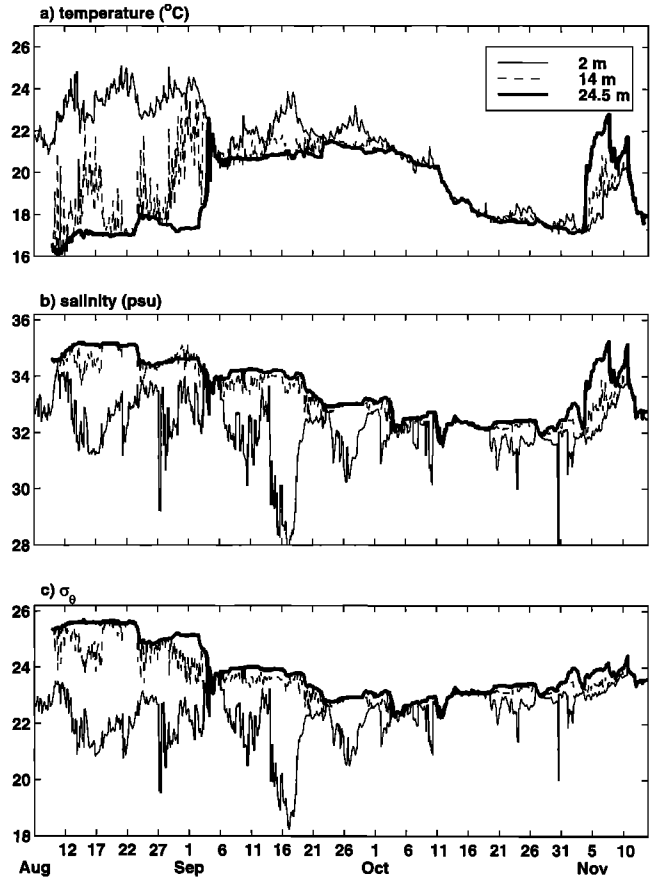

Figure 4. Time series of (a) temperature, (b) salinity, and (c) σ_θ for depths below the surface of 2, 14, and 24.5 m at the 26-m site.

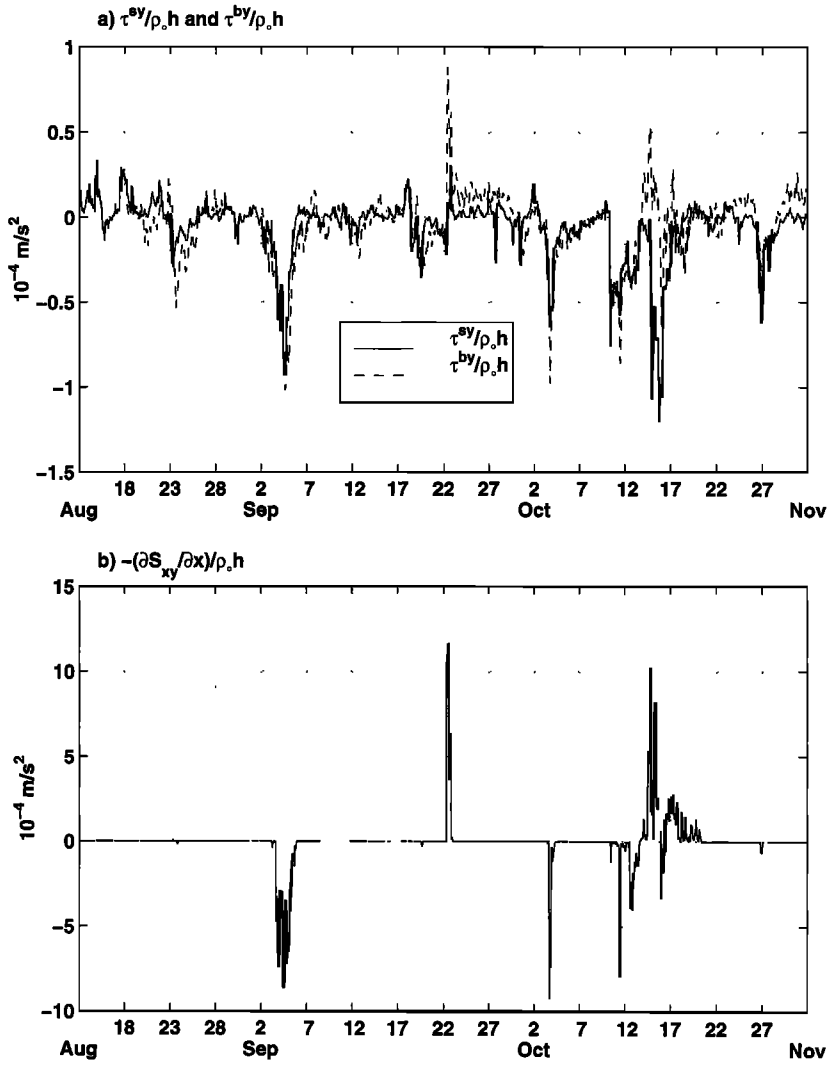

Figure 5. Time series (unfiltered hourly values) of largest terms in the along-shelf momentum balance at the 4-m site, (a) wind $\tau^{sy}/\rho_0 h$ and bottom $\tau^{by}/\rho_0 h$ stresses and (b) radiation stress gradient $-(\rho_0 h)^{-1}\,\partial S_{xy}/\partial x$. When $|\partial S_{xy}/\partial x|$ is relatively large, the site is within the surf zone. Note the vertical scales in Figures 5a and 5b differ.

of $(\rho_0 h)^{-1}\,\partial S_{xy}/\partial x$ is 1–2 orders of magnitude larger than the standard deviations of other terms in the along-shelf momentum balance (Table 2, Figure 5). To balance $\partial S_{xy}/\partial x$ with the bottom stress, the linear drag coefficient r for the subtidal flow in the surf zone must be $r = 5 \times 10^{-3}$ m s^{-1}, 10 times larger than the nominal value of r (Figure 6). The linear drag coefficient could increase because breaking waves transfer momentum effectively to the bottom or because bottom roughness increases inside the surf zone [*Garcez-Faria et al.*, 1998]. The increase in the drag coefficient in the surf zone is qualitatively consistent with results of a more detailed examination of the along-shelf momentum balance onshore of the 8-m site using additional observations, a cross-shelf integration that reduces the effects of lateral mixing on the estimated drag coefficients, and a quadratic drag formulation that includes the effect of surface waves on the mean bottom stress [*Feddersen et al.*, 1998]. Seaward of the surf zone, the estimated $\partial S_{xy}/\partial x$ term is small (Table 2).

The estimated Coriolis force $f\tilde{u}$ is relatively small at the 4- and 8-m sites but is similar to the other terms at the 21- and 26-m sites (Table 2). However, $f\tilde{u}$ will be neglected in subsequent analysis because estimates of $f\tilde{u}$ are smaller than the estimated uncertainties (section A2) and uncorrelated between sites. Furthermore, $f\tilde{u}$ is not correlated (range 0.09 to 0.37) with the sum of the acceleration, pressure gradient, and surface and bottom stresses. In contrast, the acceleration term,

Table 2. Standard Deviations of Terms in the Along-Shelf Momentum Balance (2)

Site	$\partial\tilde{v}/\partial t$	$f\tilde{u}$	$(1/\rho_0)(\partial P/\partial y)$	$\tau^{sy}/\rho_0 h$	$\tau^{by}/\rho_0 h$	$(1/\rho_0 h)(\partial S_{xy}/\partial x)$
4 m	0.2	0.2	0.3	0.9	1.2	0.1 (12.9)
8 m	0.3	0.1	···	0.8	0.7	0.1 (0.1)
13 m	0.3	0.2	···	0.4	0.4	0.0
21 m	0.2	0.2	0.3	0.4	0.3	0.0
26 m	0.2	0.2	···	0.3	0.2	0.0

Statistics for the 4- and 8-m sites are for periods when these sites were seaward of the surf zone. The values in parentheses include all periods. Units are 10^{-5} m/s^2.

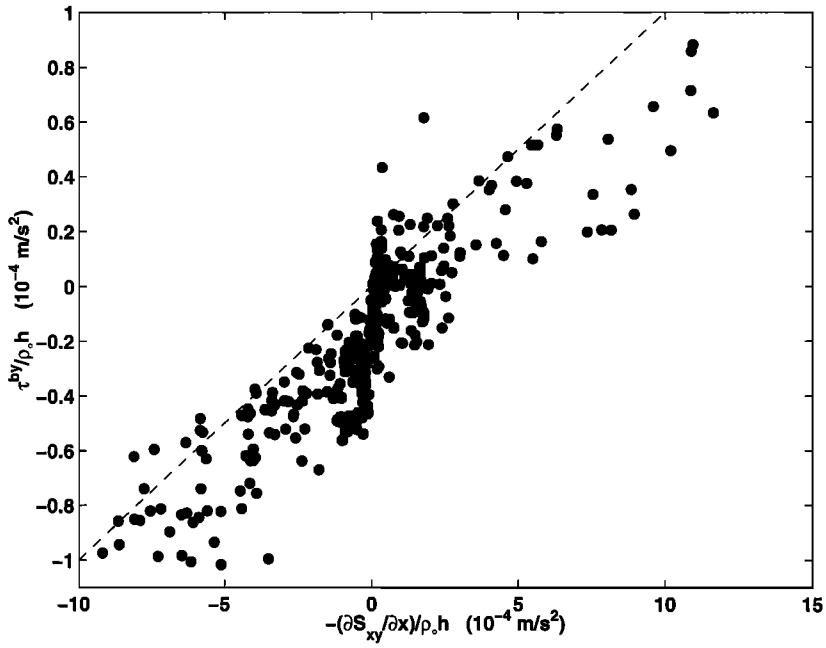

Figure 6. Hourly values of along-shelf stresses $\tau^{by}/\rho_0 h$ versus $-(\rho_0 h)^{-1}\ \partial S_{xy}/\partial x$ when the 4-m site is within the surf zone. The linear relationship and the slope of 0.1 suggest the linear drag coefficient r within the surf zone is 10 times larger than seaward of the surf zone.

which has similar magnitudes, is correlated (range 0.55 to 0.80) with the sum of Coriolis and surface and bottom stress terms at all but the 4-m site (correlation 0.36). These results are consistent with previous studies [*Allen and Smith*, 1981; *Lentz and Winant*, 1986; *Pettigrew*, 1981; *Lentz*, 1994] and suggest $f\tilde{u}$ is not estimated accurately from the observations.

When the 4-m site is offshore of the surf zone, the standard deviations of the surface wind and bottom stresses are at least 3 times as large as the other terms (Table 2) and correlated with a regression coefficient near 1.0 (Table 3). Time series of surface and bottom stress are correlated at all sites (Table 3). However, standard deviations of $\partial\bar{v}/\partial t$ and $\partial P/\partial y$ become increasingly significant as the depth increases and $\tau^{sy}/(\rho_0 h)$ and $\tau^{by}/(\rho_0 h)$ decrease (Table 2). At the 8-m site the standard deviation of the along-shelf flow acceleration and pressure gradient (measured along the 5-m isobath) are similar in magnitude but are only about half the magnitude of the surface and bottom stress terms (Table 2). The $\partial P/\partial y$ term along the 21-m isobath and the acceleration and stress terms at the 13-, 21-, and 26-m sites are all of similar magnitude (Table 2, Figure 7).

When the along-shelf pressure gradient is largest, the surface and bottom stresses differ substantially (mid August, September 5, October 16 in Figure 7). The salinity observations indicate the positive $\partial P/\partial y$ events in August that drive a southeastward flow are associated with the Chesapeake Bay plume [*Rennie et al.*, this issue]. The along-shelf momentum balance approximately closes at each site. The sum of the response terms $[\partial\bar{v}/\partial t + (\rho_0 h)^{-1}\tau^{by}]$ is well correlated with the sum of the two forcing terms $[-\rho_0{}^{-1}\ \partial P/\partial y + (\rho_0 h)^{-1}\tau^{sy}]$ at each site, and the regression coefficients are about 1.0 (Figure 8, Table 3). Furthermore, at each site these correlations are higher than the correlations between the surface and bottom stress alone.

Along the 5-m isobath the standard deviation of the barotropic pressure gradient is about 5 times larger than the standard deviation of the baroclinic component. In contrast, along the 21-m isobath the standard deviation of the barotropic pressure gradient is about twice the baroclinic component and the baroclinic component tends to oppose the barotropic component. The baroclinic pressure gradient results primarily from

Table 3. Results of Linear Regression Analysis of Forcing, $F = (-\partial P/\partial y)/\rho_0 + \tau^{sy}/(\rho_0 h)$, With Response, $R = \partial\bar{v}/\partial t + \tau^{by}/(\rho_0 h)$, in Along-Shelf Momentum Balance of the Form $R = aF + b$

	$\tau^{by}/(\rho_0 h)$ versus $\tau^{sy}/(\rho_0 h)$			R Versus F		
Site	a	b	Correlation	a	b	Correlation
4 m	0.94 ± 0.46	0.08 ± 0.41	0.69	0.98 ± 0.36	0.01 ± 0.38	0.82
8 m	0.71 ± 0.25	−0.13 ± 0.20	0.78	0.86 ± 0.20	−0.02 ± 0.18	0.89
13 m	0.63 ± 0.18	−0.06 ± 0.10	0.80	0.88 ± 0.17	0.02 ± 0.10	0.91
21 m	0.54 ± 0.16	0.01 ± 0.06	0.72	0.75 ± 0.17	0.08 ± 0.08	0.88
26 m	0.56 ± 0.17	0.01 ± 0.05	0.73	0.78 ± 0.15	0.08 ± 0.05	0.87

Results of regression between $\tau^{sy}/(\rho_0 h)$ and $\tau^{by}/(\rho_0 h)$ are also given. Analysis includes only periods when sites are seaward of the surf zone. All correlations are different from zero at the 95% confidence level, and 95% confidence levels for a and b are shown. Units are 10^{-5} m s^{-2} for intercepts.

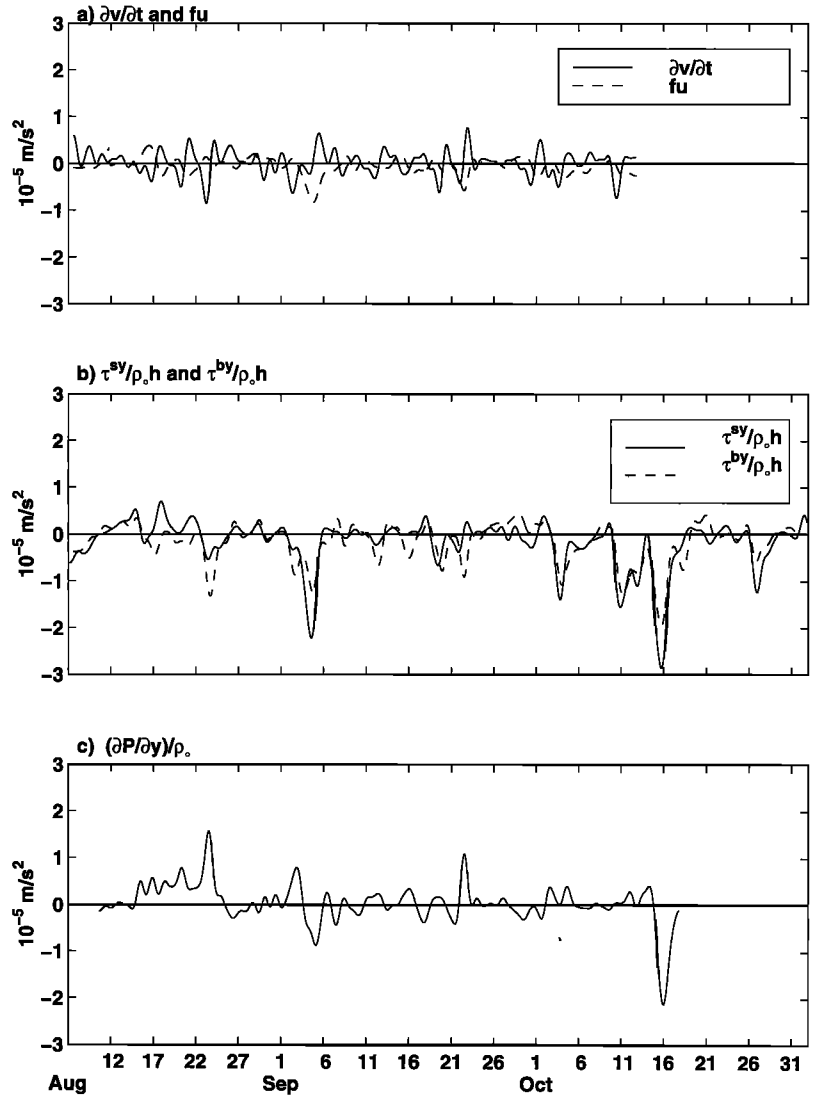

Figure 7. Time series of largest terms in the along-shelf momentum balance at the 13-m site, (a) acceleration $\partial\tilde{v}/\partial t$ and Coriolis force $f\tilde{u}$, (b) wind stress $\tau^{sy}/\rho_0 h$ and bottom stress $\tau^{by}/\rho_0 h$, and (c) pressure gradient $\rho_0^{-1}\,\partial P/\partial y$ (along the 5-m isobath; see section A1).

salinity variations and is substantial even when the water column is not stratified (e.g., early October). These estimates indicate that, at least along the 21-m isobath at this site, density estimates are critical for accurate estimation of along-shelf pressure gradients.

3.2. Cross-Shelf Momentum Balance

In the surf zone the standard deviation of $(\rho_0 h)^{-1}\,\partial S_{xx}/\partial x$ is several orders of magnitude larger than standard deviations of the other terms in the cross-shelf momentum balance (Table 4). Presumably, $\partial S_{xx}/\partial x$ is balanced by a cross-shelf pressure gradient $\partial P/\partial x$, consistent with wave-driven setup. This balance cannot be confirmed because pressure gradients were not measured accurately in this region (section A2). However, analysis of a 3.5-year-long time series (including the period of this study) of pressure in 2- and 8-m depth at the Duck site indicates that large negative $\partial S_{xx}/\partial x$ across the surf zone are balanced by $\partial P/\partial x$, consistent with wave setup (S. J. Lentz and B. Raubenheimer, submitted manuscript, 1998).

When the 4-m site is offshore of the surf zone, the standard deviation of $(\rho_0 h)^{-1}\,\partial S_{xx}/\partial x$ is an order of magnitude smaller than when the site is within the surf zone but is still an order of magnitude larger than the standard deviations of the other estimated terms, suggesting that $\partial P/\partial x$ is dominated by (unmeasured) wave setdown. At the 8-m site the magnitude of $(\rho_0 h)^{-1}\,\partial S_{xx}/\partial x$ is a factor of 3 larger than $f\tilde{v}$ and the cross-shelf wind stress term $(\rho_0 h)^{-1}\tau^{sx}$ (Table 4, Figure 9). The Coriolis force $f\tilde{v}$ and the cross-shelf wind stress τ^{sx} are positively correlated (Figure 9a). The strongest winds are from the northeast and drive an equatorward, along-shelf current with an onshore directed Coriolis force that reinforces the onshore component of the wind stress, so that the largest magnitudes of $f\tilde{v}$ and $(\rho_0 h)^{-1}\tau^{sx}$ are negative and occur concurrently (Figure 9a). However, the 8-m site is usually seaward of the surf zone and the wave-driven setdown ($\partial S_{xx}/\partial x$ is negative) opposes and is partially balanced by the wind and Coriolis forced setup during nor'easters (Figure 9b). Pressure gradients $-\rho_0^{-1}\,\partial P/\partial x = -(\rho_0 h)^{-1}\,\partial S_{xx}/\partial x + f\tilde{v} + (\rho_0 h)^{-1}\tau^{sx}$ during these events should be smaller than those from wave setdown alone and should have sign opposite to those from $f\tilde{v} + (\rho_0 h)^{-1}\tau^{sx}$ alone. Again, accurate

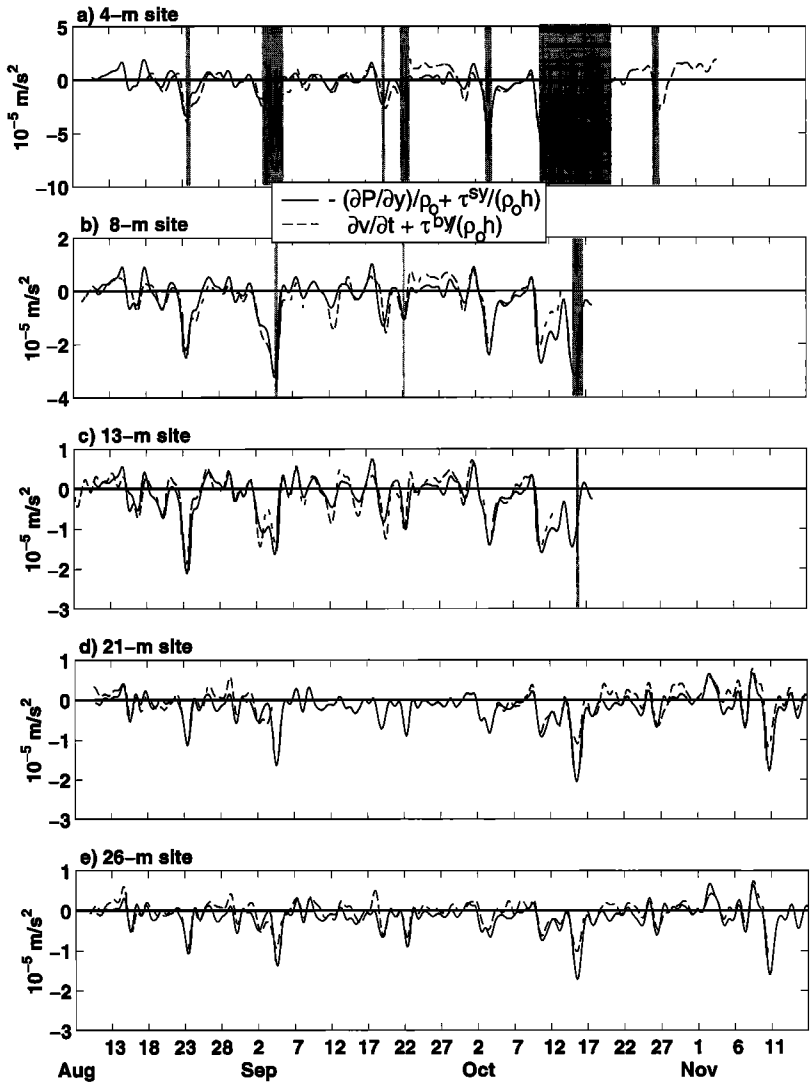

Figure 8. Time series of the along-shelf forcing $[\tau^{sy}/(\rho_0 h) - (\partial P/\partial y)/\rho_0]$ and the response $[\partial \bar{v}/\partial t + \tau^{by}/(\rho_0 h)]$ at (a) 4-m, (b) 8-m, (c) 13-m, (d) 21-m, and (e) 26-m mooring sites. The bottom stress τ^{by} is estimated using the r value seaward of the surf zone (equation (9)), and $\partial S_{xy}/\partial x$ is not included in the forcing. Thus, when a site is within the surf zone (shaded regions), discrepancies may be large.

estimates of the cross-shelf pressure gradient are needed to confirm this balance. Inside the surf zone, $\partial S_{xx}/\partial x$ is positive, and during a nor'easter, wave setup is reinforced by the cross-shelf wind stress and Coriolis force. However, the $\partial S_{xx}/\partial x$ term is so much larger than the other terms that they are likely negligible for most surf zone conditions (see section 4.2).

The cross-shelf pressure gradient $\partial P/\partial x$ was measured at the 13-m site and is balanced by $(\rho_0 h)^{-1}\,\partial S_{xx}/\partial x$ and $f\bar{v}$. The cross-shelf wind stress term $\tau^{sx}(\rho_0 h)^{-1}$ is reduced by about 40% at the 13-m site relative to the 8-m site owing to the increase in water depth (Figure 10a, Table 4). As in 8-m depth, $-(\rho_0 h)^{-1}\,\partial S_{xx}/\partial x$ and $f\bar{v} + (\rho_0 h)^{-1}\tau^{sx}$ are opposed during the strongest events, and in 13-m depth, cancellation is nearly complete in some cases (e.g., September 5 and October 4 and 10–11 in Figure 10b). The observed pressure gradients are qualitatively consistent with this cancellation (Figure 10c). The

Table 4. Standard Deviations of Terms in the Cross-Shelf Momentum Balance (1)

Site	$\partial\bar{u}/\partial t$	$f\bar{v}$	$(1/\rho_0)(\partial P/\partial x)$	$\tau^{sx}/\rho_0 h$	$\tau^{bx}/\rho_0 h$	$(1/\rho_0 h)(\partial S_{xx}/\partial x)$
4 m	0.0	1.1	···	0.9	0.4	9.6 (221.5)
8 m	0.0	1.7	···	0.8	0.2	3.6 (3.5)
13 m	0.0	1.6	2.1	0.4	0.1	1.5
21 m	0.0	1.4	1.8	0.3	0.1	0.2
26 m	0.1	1.1	1.4	0.3	0.1	0.6

Statistics for the 4- and 8-m sites are for periods when these sites were seaward of the surf zone. The values in parentheses include all periods. Units are 10^{-5} m s^{-2}.

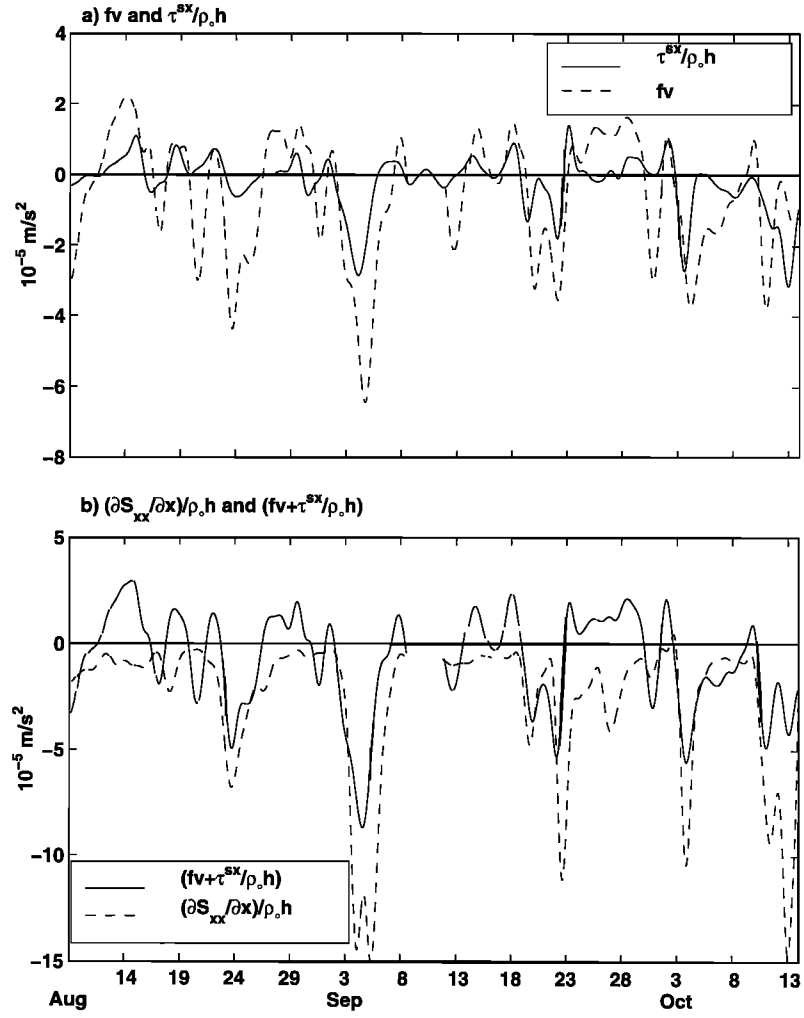

Figure 9. Time series of largest terms in the cross-shelf momentum balance at the 8-m site, (a) Coriolis force $f\bar{v}$ and wind stress $\tau^{sx}/\rho_0 h$ and (b) radiation stress gradient $(\rho_0 h)^{-1}\ \partial S_{xx}/\partial x$ and $(f\bar{v} + \tau^{sx}/\rho_0 h)$. Note the vertical scales differ in Figures 9a and 9b.

Coriolis force $f\bar{v}$, $\partial S_{xx}/\partial x$, and $\partial P/\partial x$ are mutually correlated. Linear regression of $f\bar{v}$ and $\rho_0^{-1}\ \partial P/\partial x$ yields a significant correlation (0.63) and a regression coefficient of 0.82 (Table 5), suggesting a geostrophic balance. However, $\rho_0^{-1}\ \partial P/\partial x$ is better correlated (0.80) with $[f\bar{v} - (\rho_0 h)^{-1}\ \partial S_{xx}/\partial x]$ than with $f\bar{v}$ alone. These results (Tables 4 and 5, Figures 9 and 10) suggest that $\partial S_{xx}/\partial x$ is important in the cross-shelf momentum balance offshore of the surf zone, in depths at least as great as 13 m.

At the 21- and 26-m sites, $f\bar{v}$ and $\rho_0^{-1}\ \partial P/\partial x$ are highly correlated with linear regression coefficients near 1 (Table 5) and are larger than the other terms (Table 4). The cross-shelf momentum balance is thus consistent with geostrophy (Figure 11). The standard deviations of $\tau^{sx}/\rho_0 h$ and $(\rho_0 h)^{-1}\ \partial S_{xx}/\partial x$ are less than 1/5 of $f\bar{v}$ in 21-m depth (Table 4), and the correlation between $f\bar{v}$ and $\rho_0^{-1}\ \partial P/\partial x$ is not altered significantly by including either in the balance. At the 26-m site the standard deviation of the estimated $(\rho_0 h)^{-1}\ \partial S_{xx}/\partial x$ is larger (about 1/2 of $f\bar{v}$) than at the 21-m site because the local bottom slope is steeper (h_x in (15), discussed below). However, the correlation is not increased by including $\partial S_{xx}/\partial x$, possibly because of the disparity in the spatial scales used to estimate $\partial S_{xx}/\partial x$ and $\partial P/\partial x$. The local bottom slope in 26-m depth is used to estimate $\partial S_{xx}/\partial x$, but the local slope is larger and of different sign than the average bottom slope over the cross-shelf separation of the pressure gauges (at the 5- and 33-m sites) used to estimate $\partial P/\partial x$ at the 26-m site (Figure 2).

The baroclinic component of the cross-shelf pressure gradient often opposes the barotropic component at the 13- and 21-m sites, where bottom pressure gradient and density gradient estimates could be made (Figure 12). Correlations between the barotropic and baroclinic pressure gradients are −0.82 at both sites. The standard deviations indicate that the depth-averaged baroclinic pressure gradient balances 30–45% of the barotropic pressure gradient. Cross-shelf density gradients (baroclinic pressure gradients) in October, when stratification is relatively weak (Figure 4), are similar in magnitude to cross-shelf density gradients in August, when stratification is relatively strong (Figure 12).

The importance of the baroclinic contribution to the depth-averaged, cross-shelf pressure gradient and the tendency for a geostrophic balance suggest the vertical shear in the along-shelf velocity may be in thermal wind balance over the inner shelf,

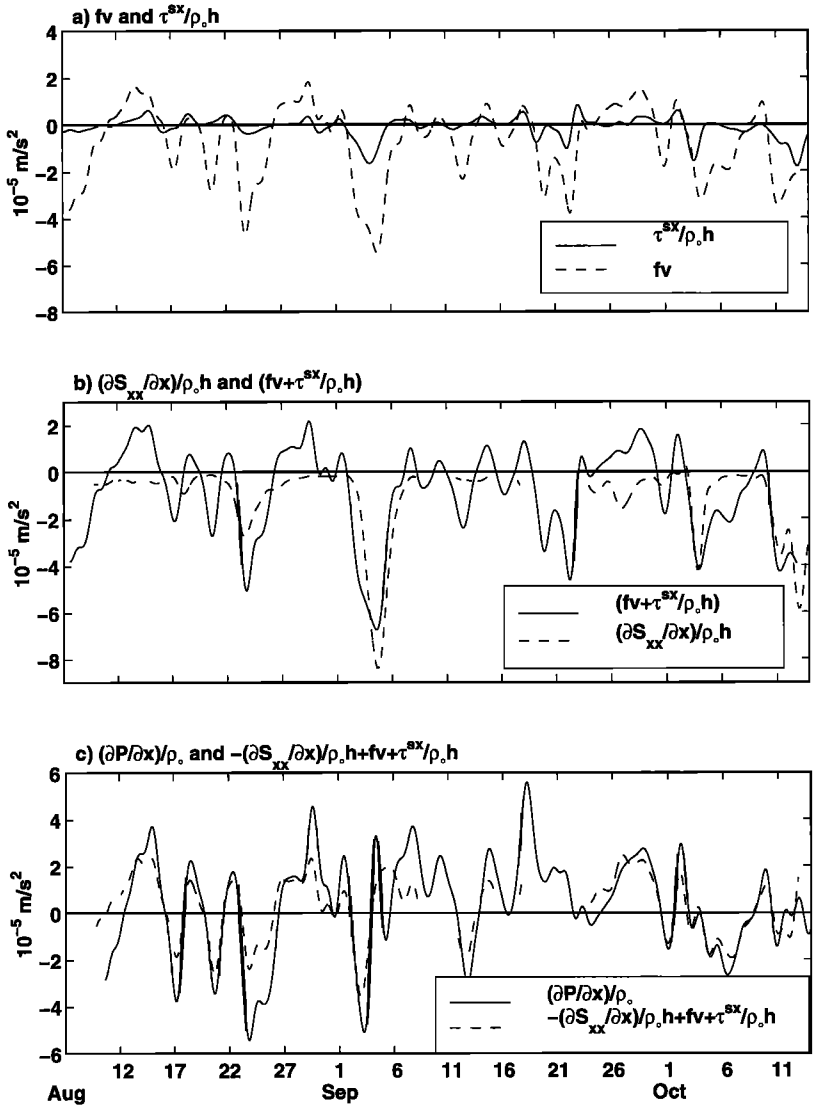

Figure 10. Time series of largest terms in the cross-shelf momentum balance at the 13-m site, (a) Coriolis force $f\bar{v}$ and wind stress $\tau^{sx}/\rho_0 h$, (b) radiation stress gradient $(\rho_0 h)^{-1}\,\partial S_{xx}/\partial x$ and $(f\bar{v} + \tau^{sx}/\rho_0 h)$, and (c) pressure gradient $\rho_0^{-1}\,\partial P/\partial x$ and $[f\bar{v} + \tau^{sx}/\rho_0 h - (\rho_0 h)^{-1}\,\partial S_{xx}/\partial x]$. Correlations and regression coefficients are given in Table 5.

$$\frac{\partial v}{\partial z} = -\frac{g}{\rho_0 f}\frac{\partial \rho}{\partial x}. \tag{6}$$

Although (6) has been shown to hold in the middle of the water column at midshelf [*Winant et al.*, 1987], it is not obvious that this balance will hold over the shallow inner shelf, where no part of the water column is distant from the surface and bottom. The moored array observations provide five locations where the two terms in this balance can be compared (Table 6). In each case, $\partial\rho/\partial x$ is estimated as the difference between densities at the same depth on adjacent moorings divided by the mooring separation. (Density at 4.4-m depth for the 13-m site was computed by linearly interpolating between the 1.5- and 7.6-m densities, Figure 2.) Vertical shears $\partial v/\partial z$, estimated from current meters vertically bracketing the $\partial\rho/\partial x$ at both moorings, are substantial, corresponding to along-shelf velocity differences of 15–40 cm s^{-1} across the water column.

The vertical shear in the middle of the water column is approximately in thermal wind balance (Table 6, Figure 13). Standard deviations of the two terms in (6) are roughly equal at each location and increase toward the coast, consistent with strong cross-shelf density gradients in the vicinity of the 8- and 13-m sites owing to the Chesapeake Bay plume and, during August, to upwelling/downwelling of the pycnocline. The two

Table 5. Regression Analysis of $f\bar{v}$ With $(\partial P/\partial x)/\rho_0$ Terms in Cross-Shelf Geostrophic Balance

Site	Correlation Coefficient	Regression Coefficient	Days
13 m	0.63	0.82 ± 0.38	63
13 m*	0.80	1.34 ± 0.41	48
21 m	0.92	1.16 ± 0.22	50
26 m	0.93	1.19 ± 0.15	78

All correlations are significantly different from zero at the 95% confidence level, and 95% confidence intervals for regression coefficients are shown.

*Regression analysis of $f\bar{v} - \partial S_{xx}/\partial x$ is with $(\partial P/\partial x)/\rho_0$.

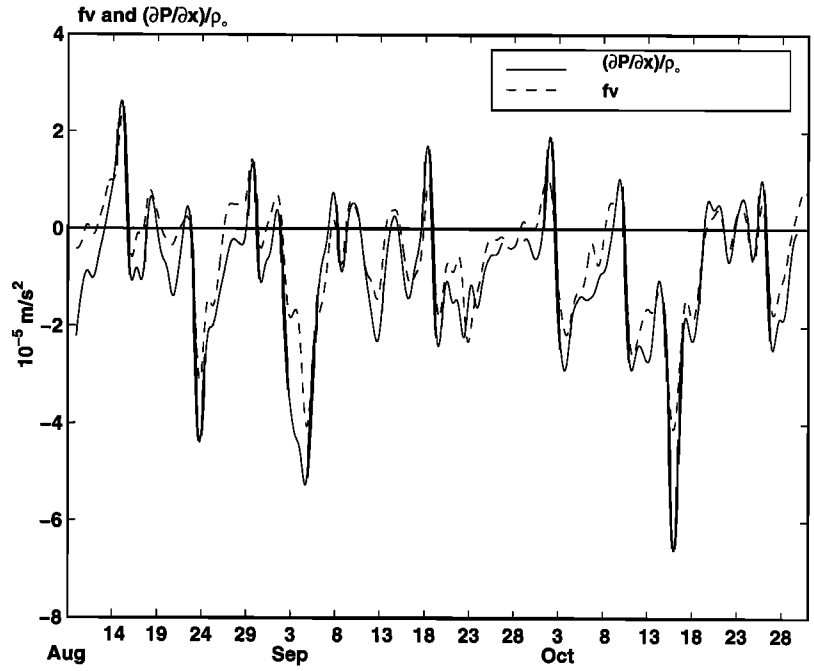

Figure 11. Time series of largest terms in the cross-shelf momentum balance at the 26-m site, $f\tilde{v}$ and ρ_0^{-1} $\partial P/\partial x$. Correlations and regression coefficients between $f\tilde{v}$ and ρ_0^{-1} $\partial P/\partial x$ are given in Table 5.

terms in (6) are correlated at all sites. Inaccuracies in the interpolation of density at the 13-m site may contribute to the lower correlations for the 8- and 13-m pair. The large separation between the 21- and 26-m sites (10 km) relative to the cross-shelf scale of the plume (estimated from shipboard surveys) probably contributes to the lower correlations for this pair. Despite the difficulties of comparing vertical shears estimated at pairs of mooring sites with finite difference estimates of the density gradient between mooring sites, the observations indicate that much of the subtidal vertical shear variability is in thermal wind balance in depths as shallow as 10 m.

4. Discussion

The momentum balances suggest three distinct dynamical regions: the surf zone, inner shelf, and midshelf. In the surf zone, forcing by wave radiation stress gradients dominates both along-shelf and cross-shelf momentum balances. Over the in-

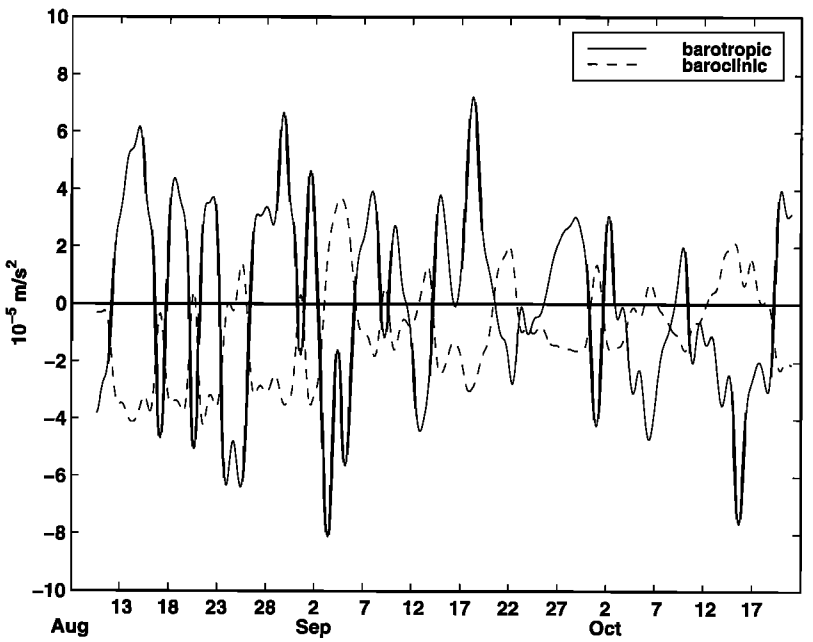

Figure 12. Time series of the barotropic and baroclinic contributions to the depth-averaged, cross-shelf pressure gradient (see (3)) at the 13-m site.

Table 6. Comparison of Terms in Thermal Wind Balance, Equation (6)

Mooring Sites	Meters Below Surface	Standard Deviations $\frac{-g}{\rho_0 f}$	Standard Deviations $\frac{\partial \rho}{\partial x}$	Correlation Coefficient	Days
8–13	4.4	3.6	3.3	0.65	49
13–21	7.6	2.5	2.5	0.89	31
13–21	12.7	1.1	0.9	0.72	53
21–26	7.6	0.9	1.1	0.62	65
21–26	12.7	0.8	0.6	0.53	62

Standard deviation units are 10^{-2} s^{-1}. All correlations are significantly different from zero at the 95% confidence level.

ner shelf, offshore of the surf zone to about the 13-m isobath, the along-shelf momentum balance is primarily between surface wind and bottom stresses, with along-shelf pressure gradients usually a smaller contribution. The cross-shelf momentum balance is between cross-shelf pressure gradients, wave radiation stress gradients, Coriolis forces, and, to a lesser extent, cross-shelf wind stresses. At the midshelf 21- and 26-m sites the along-shelf balance is between wind stresses, along-shelf pressure gradients, bottom stresses, and accelerations. The cross-shelf momentum balance is geostrophic. These simplified momentum balances are used here to examine the relationship between the forcing (winds, waves, and along-shelf pressure gradients) and the response (along-shelf currents and cross-shelf pressure gradients) and to derive simple scalings relevant to other locations. The along-shelf pressure gradient $\partial P/\partial y$ is treated as a forcing rather than as a response because the observed $\partial P/\partial y$ (along both the 5- and 21-m isobaths) are not correlated with the local wind stress. As indicated in section 3.1, part of the variability in $\partial P/\partial y$ along the 5-m isobath is associated with the Chesapeake Bay plume events [*Rennie et al.*, this issue], and some of the variability is likely also a response to the large-scale wind field [*Wang*, 1979; *Noble and Butman*, 1979; *Yankovsky and Garvine*, 1998]. In either case, $\partial P/\partial y$ is driven by large-scale processes not included in the present forcing terms.

4.1. Along-Shelf Velocity Response

The depth-averaged, along-shelf momentum balance (2) is recast here to relate the depth-averaged, along-shelf velocity to the forcing

$$\frac{\partial \bar{v}}{\partial t} + \frac{r\bar{v}}{h} \simeq -\frac{1}{\rho_0}\frac{\partial P}{\partial y} + \frac{\tau^{sy}}{\rho_0 h} - \frac{1}{\rho_0 h}\frac{\partial S_{xy}}{\partial x}. \tag{7}$$

It has been assumed that turbulent Reynold's stresses, nonlinear advective terms, and the Coriolis term $f\bar{u}$ (see section 3.1) are small; a linear drag law ((5) and section A3) provides an accurate estimate of the bottom stress ($(\rho_0 h)^{-1}\tau^{by}$ in (2)); and the near-bottom, along-shelf velocity v_b is approximately equal to, or at least well correlated with, the depth-averaged, along-shelf velocity $\bar{v}$. At each site, v_b and $\bar{v}$ are well correlated (0.86 to 0.99) and v_b ranges from $0.5\bar{v}$ to $0.8\bar{v}$ based on a linear regression analysis. Given that v_b and $\bar{v}$ are well correlated, the difference in magnitude may be accounted for by adjusting r.

Integrating (7) in time yields [*Lentz and Winant*, 1986]

$$\bar{v}_P = \int_{t_0}^{t}\left(-\frac{1}{\rho_0}\frac{\partial P}{\partial y} + \frac{\tau^{sy}}{\rho_0 h} - \frac{1}{\rho_0 h}\frac{\partial S_{xy}}{\partial x}\right)e^{-(t-t')/T_f}\,dt' + \bar{v}_0 e^{-(t-t_0)/T_f} \tag{8}$$

where $T_f = h/r$ is a frictional timescale and $\bar{v}_0 = \bar{v}(t = t_0)$. On the basis of (7) or (8), two factors determine the character of $\bar{v}$ and its cross-shelf structure, the relative magnitudes of the forcing terms and the forcing timescale relative to the frictional timescale T_f. As noted above, $\partial S_{xy}/\partial x$ dominates the along-shelf forcing in the surf zone. Seaward of the surf zone,

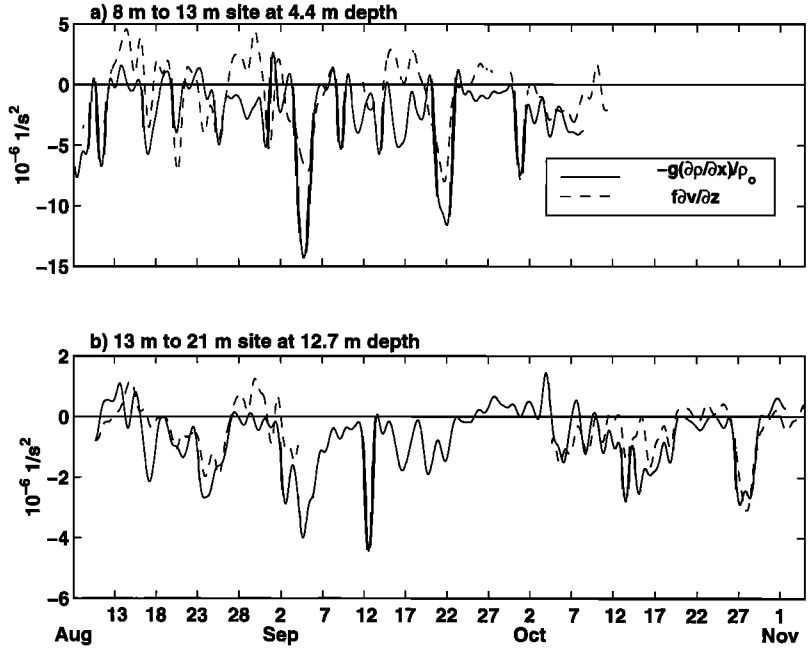

Figure 13. Time series of the terms in the thermal wind balance (6) between the (a) 8- and 13-m sites (4.4 m below surface) and (b) 13- and 21-m sites (12.7 m below surface). Correlations are given in Table 6.

$\partial S_{xy}/\partial x$ is small and the relative importance of τ^{sy}/h and $\partial P/\partial y$ depends on their cross-shelf structure. In the absence of cross-shelf variations, $\partial P/\partial y$ will become increasingly more important relative to τ^{sy}/h as the depth increases [e.g., *Lentz and Winant*, 1986], and this is qualitatively true in the present observations (compare the cross-shelf variation of τ^{sy}/h with that of $\partial P/\partial y$ in Table 2).

If the forcing varies on timescales that are long compared with T_f, then the response is basically frictional. The along-shelf flow is approximately in phase with the forcing and quasi-steady in the sense that the accelerations are dynamically negligible. In this case, from (7), $\bar{v}_P \simeq T_f[-\rho_0^{-1}\,\partial P/\partial y + \tau^{sy}/\rho_0 h + (\rho_0 h)^{-1}\,\partial S_{xy}/\partial x]$. In contrast, if the forcing timescale is short compared to T_f, then the response lags the forcing and is weaker than the steady response. The three forcing terms (sampled hourly) have decorrelation timescales of 1–2 days. The results in section 3 suggest that roughly

$$r = 5 \times 10^{-3}\ \text{m s}^{-1} \qquad h \le 3.0H_{sig} \tag{9a}$$

(within the surf zone),

$$r = 5 \times 10^{-4}\ \text{m s}^{-1} \qquad h > 3.0H_{sig} \tag{9b}$$

(seaward of the surf zone).

Within the surf zone, assuming $h = 8$ m or less, T_f is 30 min or less, short compared with the forcing timescale and consistent with previous observations in which surf zone flows responded within a few hours to changes in forcing [*Feddersen et al.*, 1998]. Seaward of the surf zone, $h = 4 - 26$ m and (9) implies $T_f = 2$–14 hours. Thus, at midshelf, T_f approaches the forcing decorrelation timescale and the flow response may detectably lag the forcing. The observed time lags for maximum correlation between subtidal flow $\bar{v}$ and forcing $(-\partial P/\partial y + \tau^{sy}/h + h^{-1}\,\partial S_{xy}/\partial x)$ are 2, 7, and 9–11 hours for the 4-, 8-m, and deeper sites, respectively. The increase in the magnitude of the lags with increasing water depth is consistent with (7) and (9).

Estimates of $\bar{v}_P$ from the forcing were made using (8) and the prescription for r in (9). The frictional timescale T_f in the surf zone is shorter than the hourly sample rate, therefore $\bar{v}_P$ was set equal to the forcing times T_f when the 4- or 8-m sites were in the surf zone. Unfiltered hourly time series of $\bar{v}_P$ and observed $\bar{v}$ for each site are similar (Plate 1). Root-mean-square (rms) differences are about 10 cm s^{-1}, correlations are 0.74 to 0.86, and linear regression slopes range from 0.92 to 1.20.

The $\bar{v}_P$ estimates reproduce the observed cross-shelf variations in $\bar{v}$. For example, on August 20 and 23, strong along-shelf currents are driven in part by an along-shelf pressure gradient associated with the Chesapeake Bay plume (section 3.1). The observed and predicted currents are maximum at the 13-m site (about -40 and -70 cm s^{-1} on August 20 and 23, respectively). Flows are weaker at the 21- and 26-m sites because the pressure gradient associated with the plume does not extend offshore to these sites. The pressure gradient is present onshore of the 13-m site, but the response decreases as the depth decreases from 13 to 4 m because the pressure gradient body force is balanced by bottom stress (e.g., $r\bar{v}_P \simeq h\,\partial P/\partial y$ from (7)). The estimated velocity $\bar{v}_P$ does not reproduce $\bar{v}$ as well during a similar plume event around September 20, probably because the array does not resolve cross-shelf variations in $\partial P/\partial y$ during this event. The $\bar{v}_P$ estimates using the bottom stress formulation (9) do reproduce the flow reversal on September 22 (when $\partial S_{xy}/\partial x$ opposes the wind) between the surf zone ($\bar{v} = +80$ cm s^{-1} at the 4-m site) and the inner shelf ($\bar{v} = -50$ cm s^{-1} at the 13-m site). The flow reversal observed between the 4- and 21-m sites on October 14–15 is also predicted. The crude drag formulation (9) contributes to errors in the magnitude of $\bar{v}_P$ in the transition region between the surf zone and the inner shelf. Errors in the sign of $\bar{v}_P$ (e.g., at the 8-m site on September 22, where $\bar{v}_P = +15$ cm s^{-1} and $\bar{v} = -30$ cm s^{-1}) may occur because of inaccurate estimation of the small residual stress when opposing stresses from wave breaking and wind are about equal.

Overall, these comparisons (e.g., Plate 1) suggest that (8) estimates $\bar{v}$ well, given the forcing and the prescription (9) for the bottom drag coefficient. It is somewhat surprising that the linear drag formulation (9) works this well, given its likely dependence on waves, bottom roughness, and stratification. To determine the sensitivity of $\bar{v}_P$ to variations in r (seaward of the surf zone), the rms difference between $\bar{v}_P$ and $\bar{v}$ was computed as a function of r over the range 1–20 $\times 10^{-4}$ m s^{-1}. Seaward of the surf zone, the rms error is not sensitive to r between 3 and 6 $\times 10^{-4}$ m s^{-1}. The rms difference is more sensitive to low values of r than to high values. Clearly, bottom stress remains a poorly understood aspect of the surf zone and inner shelf dynamics.

4.2. Cross-Shelf Pressure Gradient Response

The cross-shelf pressure gradient balances wave, wind, and Coriolis (associated with the along-shelf flow) forces

$$\frac{\partial P}{\partial x} \simeq -\frac{1}{h}\frac{\partial S_{xx}}{\partial x} + \frac{\tau^{sx}}{h} + \rho_0 f\bar{v}. \tag{10}$$

Over midshelf the present (section 3.2) and previous results indicate that the cross-shelf balance (10) is approximately geostrophic. However, as the depth decreases, the cross-shelf wind and radiation stresses become more important. The cross-shelf gradient of the depth-averaged pressure may be estimated from (10), given cross-shelf distributions of depth, wave radiation stress S_{xx}, cross-shelf wind stress, and the along-shelf current $\bar{v}$ (which may be estimated using (7) and (8), given the wave radiation stress S_{xy}, along-shelf wind stress, and along-shelf pressure gradient). If, on the inner shelf (seaward of the surf zone, where $\partial S_{xy}/\partial x$ is negligible), the wind stress is approximately equal to the bottom stress in the along-shelf momentum balance (e.g., $\bar{v} \simeq \tau^{sy}/(\rho_0 r)$ in (7); see section 3.1), then the cross-shelf pressure gradient (10) depends only on the wave radiation stress S_{xx} and the local wind stress

$$\frac{\partial P}{\partial x} \simeq -\frac{1}{h}\frac{\partial S_{xx}}{\partial x} + \frac{\tau^{sx}}{h} + \frac{f\tau^{sy}}{r}. \tag{11}$$

To examine the relative magnitude of the three terms on the right-hand side of (11), consider first the ratio of the cross-shelf wind stress to the Coriolis force is

$$\frac{\tau^{sx}/h}{f\tau^{sy}/r} = \frac{r\tan(\phi)}{fh} \tag{12}$$

where an along-shelf wind stress direction corresponds to $\phi = 0$. The depth h, where the magnitudes of the two terms are equal as a function of the wind stress orientation, for midlatitudes ($f = 10^{-4}$ s^{-1}) and a typical drag coefficient seaward of the surf zone ($r = 5 \times 10^{-4}$ m/s) are shown in Figure 14a. For winds oriented 45° relative to the coastline, as is often the case at Duck, the cross-shelf wind stress is about half the

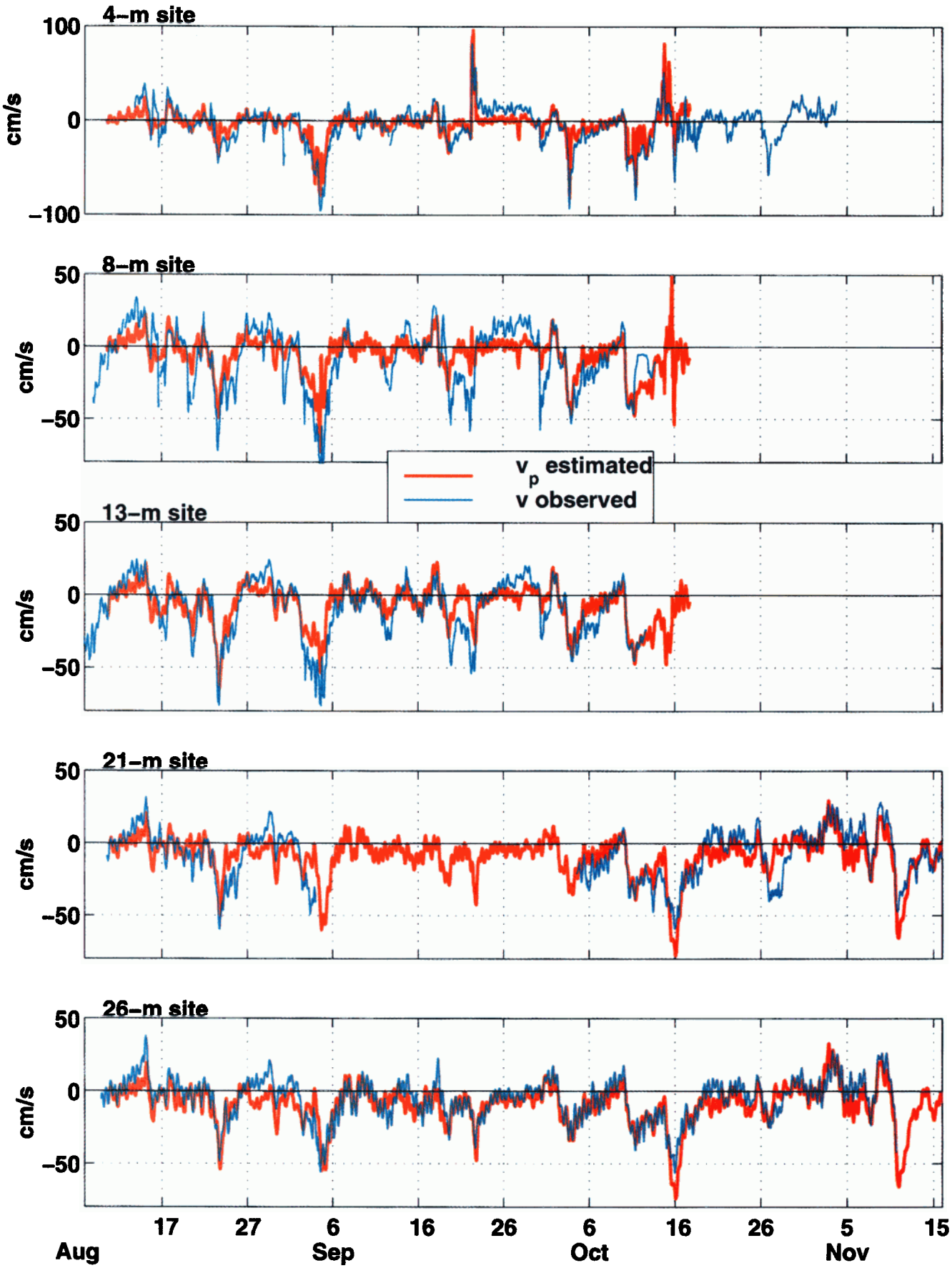

Plate 1. Time series (unfiltered hourly) of depth-averaged, along-shelf velocities at each site. Red curves are observed $\bar{v}$ and blue curves are $\bar{v}_p$ estimated from forcing using (8) and (9). The vertical scale is different for the 4-m site.

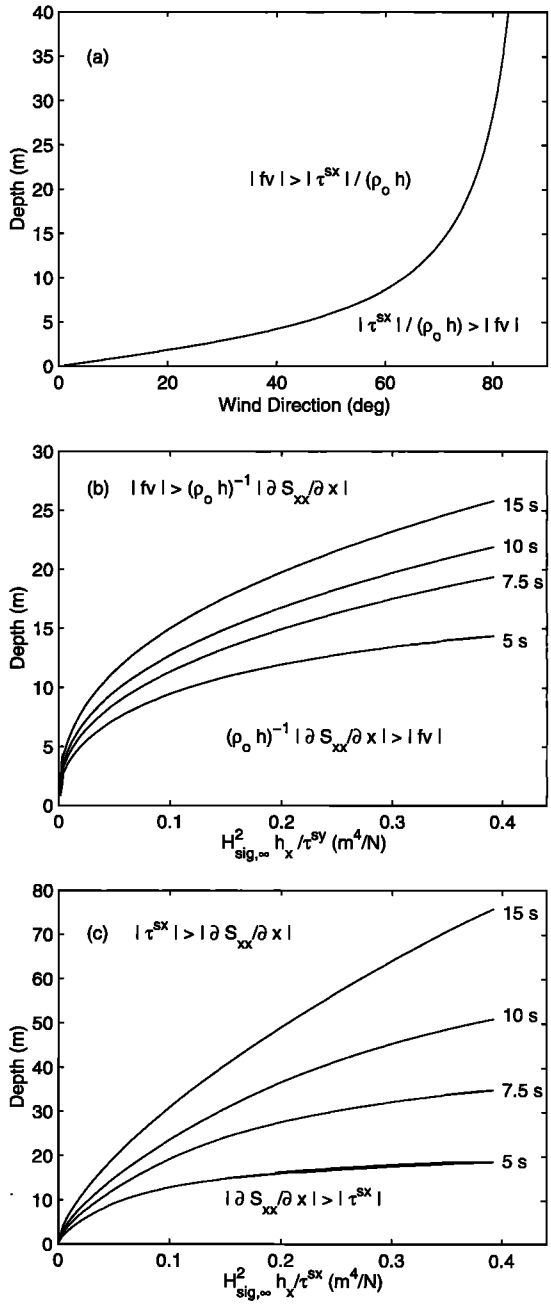

Figure 14. (a) Depth where Coriolis force associated with wind-driven, along-shelf flow $|f\bar{v}|$ equals the cross-shelf wind stress $|\tau^{sx}|/\rho_0 h$ as a function of wind direction (see (12)). An along-shelf-directed wind corresponds to 0°. (b) Depth where $|f\bar{v}|$ equals the radiation stress gradient $(\rho_0 h)^{-1}\,|\partial S_{xx}/\partial x|$, as a function of $H^2_{\text{sig},\infty}h_x/\tau^{sx}$ (see (16)). (c) Depth where $|\tau^{sx}|$ equals $|\partial S_{xx}/\partial x|$ as a function of $H^2_{\text{sig},\infty}h_x/\tau^{sx}$ (see (17)). Each curve in Figures 14b and 14c corresponds to the indicated wave period. Terms were estimated with $f = 10^{-4}$ s^{-1}, $r = 5 \times 10^{-4}$ m s^{-1}, and $\rho_0 = 1023$ kg m^{-3}.

Coriolis force in 12-m depth and the terms are approximately equal in 6-m depth (consistent with observations; see Figures 10a and 9a). The cross-shelf wind stress will be relatively more important at lower latitude or if the drag coefficient is larger.

Observational studies concluding that the cross-shelf momentum balance is primarily geostrophic are often in depths greater than 20 m and do not consider the contribution of wave-driven setdown associated with nonbreaking surface waves in variable depth. In the present observations the wave radiation stress gradients are at least as large as the cross-shelf wind stress and the Coriolis force in $O(10$ m) depth seaward of the surf zone (Figures 9b and 10b). The generality of this result is assessed by estimating the size of $h^{-1}\,\partial S_{xx}/\partial x$ relative to the Coriolis term $f\tau^{sy}/r$ and the cross-shelf wind stress τ^{sx}/h.

Assuming normally incident waves for simplicity, the radiation stress given by (A4) is

$$S_{xx} = E\left(\frac{2c_g}{c} - \frac{1}{2}\right) \tag{13}$$

where the phase speed $c = \omega/k$ and the group velocity $c_g = \partial\omega/\partial k$ follow from the linear wave dispersion equation

$$\frac{\omega^2 h}{g} = kh \tanh(kh)$$

where ω and k are the wave radian frequency and wavenumber, respectively. Energy conservation (for the present case of nonbreaking waves) yields

$$E = \frac{(Ec_g)_\infty}{c_g} = \frac{\rho_0 g H^2_{\infty,\text{sig}}}{16[\tanh(kh) + kh\,\text{sech}^2(kh)]}$$

here $H_{\infty,\text{sig}}$ is the deep water significant wave height. Substitution into (13) yields

$$S_{xx} = \frac{\rho_0 g H^2_{\infty,\text{sig}} f(s)}{16} \tag{14}$$

where $s = kh$ and

$$f(s) = \frac{1/2 + s\,\text{sech}(s)\,\text{csch}(s)}{\tanh(s) + s\,\text{sech}^2(s)}.$$

Using the dispersion equation, s depends on the nondimensional depth $\omega^2 h/g$. Differentiation yields

$$\frac{1}{h}\frac{\partial S_{xx}}{\partial x} = \frac{1}{16}\rho_0 H^2_{\infty,\text{sig}}\frac{\omega^4 h_x}{g}q(s) \tag{15}$$

where

$$q(s) = f'(s)\frac{\coth(s)}{s[\tanh(s) + s\,\text{sech}^2(s)]}.$$

The ratio of the radiation stress term to the Coriolis term is thus

$$\left(\frac{1}{h}\frac{\partial S_{xx}}{\partial x}\right)\Big/\left(\frac{f\tau^{sy}}{r}\right) = \frac{\rho_0 r}{16gf}\frac{H^2_{\text{sig},\infty}h_x}{\tau^{sy}}\omega^4 q(s). \tag{16}$$

Similar calculations for the ratio of $\partial S_{xx}/\partial x$ and τ^{sx} yield

$$\frac{\partial S_{xx}}{\partial x}\Big/\tau^{sx} = \frac{\rho_0}{16}\frac{H^2_{\text{sig},\infty}h_x}{\tau^{sx}}\omega^2 p(s) \tag{17}$$

where

$$p(s) = \frac{\omega^2 h}{g}q(s) = \frac{f'(s)}{\tanh(s) + s\,\text{sech}^2(s)}.$$

The functions q and p depend relatively strongly on $\omega^2 h/g$ (Figure 15). For example, in shallow water, $p \simeq h^{-5/2}$ and $q \simeq h^{-3/2}$. In contrast, for wind stresses that do not vary in the cross-shelf direction, the cross-shelf wind stress term τ^{sx}/h varies as h^{-1} and the Coriolis term $f\tau^{sy}/r$ is constant. These

ratios ((16) and (17)) suggest wave radiation stresses will dominate in very shallow water, even with nonbreaking waves.

The depth where the ratio of the radiation stress to the Coriolis term equals unity (from (16)) is shown in Figure 14b, for midlatitudes and a typical value of the drag coefficient ($r = 5 \times 10^{-4}$ m s^{-1}) as a function of $H^2_{sig,\infty}h_x/\tau^{sy}$ for several wave periods. At Duck, $H^2_{sig,\infty}$ and τ^{sy} are correlated such that their ratio is typically $O(20\text{–}40)$ m^4 N^{-1}. The beach slope between the 4- and 13-m sites is roughly 0.01, so $H^2_{sig,\infty}h_x/\tau^{sy} \simeq 0.2\text{–}0.4$. Wave periods are $O(10$ s), so the ratio (16) is unity in about 15- to 20-m depth (Figure 14b), qualitatively consistent with the observation that the terms are about equal in 13-m depth (Figure 10b). For fixed $H^2_{sig,\infty}h_x/\tau^{sy}$ the radiation stress term is important in deeper water as the surface wave period (and hence wavelength) increases (Figure 14b), reflecting the dependence of q on the nondimensional depth (Figure 15).

At midlatitudes, when the wind direction is not close to cross-shelf directed (e.g., when the wind direction <60° in Figure 14a), the cross-shelf wind stress exceeds the Coriolis term only when $h < 10$ m. However, the S_{xx} gradient term also usually exceeds the Coriolis term in depths less than 10 m (Figure 14b) and the S_{xx} gradient term increases rapidly as the depth decreases further (Figure 15). Under these circumstances the Coriolis force dominates on the midshelf, the Coriolis and radiation stress terms are both important on the inner shelf, and the cross-shelf wind stress is never a dominant term. In the contrasting situation of a cross-shelf wind, the Coriolis term vanishes and the cross-shelf wind stress is larger than the radiation stress term offshore (Figure 14c). The depth where τ^{sx}/h equals the radiation stress term depends on $H^2_{sig,\infty}h_x/\tau^{sx}$ and the wave period ((17) and Figure 14c). The wave radiation stress gradient from an energetic ocean swell (e.g., 15-s period waves with $H_{sig,\infty} = 3$ m) shoaling on a moderately sloping shelf (e.g., $h_x = 0.005$) will exceed the force of a strong cross-shelf wind stress (0.4 N m^{-2}, 10-m wind speed 15 m s^{-1}) in less than 30-m water depth (Figure 14c).

The above results (e.g., Figures 14b and 14c) suggest that $\partial S_{xx}/\partial x$, τ^{sx}/h, and $f\tau^{sy}/r$ may be similar in magnitude seaward of the surf zone, in depths of $O(10\text{–}30$ m). Within the surf zone, τ^{sx}/h and $f\tau^{sy}/r$ are negligible because $\partial S_{xx}/\partial x$ is orders of magnitude larger than seaward of the surf zone [*Longuet-Higgins and Stewart*, 1964; *Bowen et al.*, 1968]. Although $\partial S_{xy}/\partial x$ was neglected offshore of the surf zone (11), it can drive substantial along-shelf currents in the surf zone. Hence, in the surf zone, (10) reduces to

$$\frac{\partial P}{\partial x} \simeq -\frac{1}{h}\frac{\partial S_{xx}}{\partial x} - \frac{f}{r}\frac{\partial S_{xy}}{\partial x} \tag{18}$$

using (7) with a surf zone balance between radiation stress gradients and bottom friction. The ratio of the two terms on the right-hand side of (18) is

$$\frac{(f/r)\partial S_{xy}/\partial x}{(\partial S_{xx}/\partial x)/h} = \frac{fh}{r}\frac{\sin(2\theta)}{[\cos(2\theta) + 2]} \tag{19}$$

using (A2) and (A4), assuming shallow water waves ($c \sim c_g$) and similar cross-shelf scales for the divergences, and with $\theta = 0$ corresponding to normally incident waves.

The ratio of the frictional and Coriolis timescales ($fh/r = fT_f$) is about 0.1 for $h = 5$ m, $r = 5 \times 10^{-3}$ m s^{-1}, and $f = 10^{-4}$ s^{-1}. The other fraction involving the incident wave angle θ is always less than 0.6, and for waves within 10° of normally incident it is 0.1 or less. Thus (18) suggests that under most surf zone conditions the pressure gradient associated with wave-driven setup will be at least an order of magnitude larger than the geostrophic pressure gradient associated with the wave-driven, along-shelf current jet.

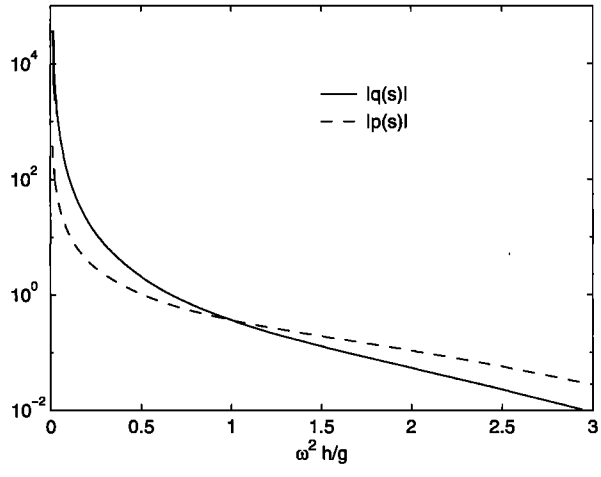

Figure 15. Functions q (see (15)) and p (see (17)) versus the nondimensional depth $\omega^2 h/g$.

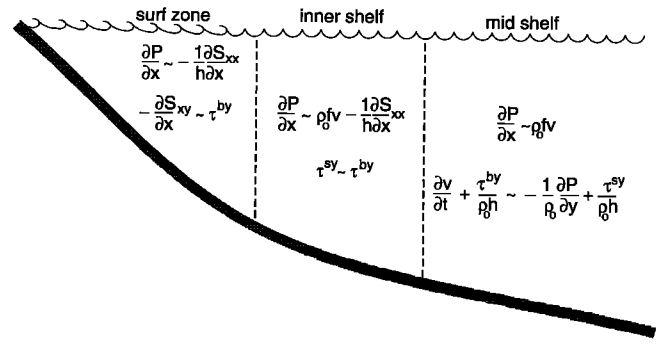

Figure 16. Summary schematic of the dominant cross-shelf and along-shelf momentum balances in the surf zone, inner shelf, and midshelf regions. Dashed lines indicate transition zones where momentum balances may be more complicated.

5. Summary

Estimates of terms in the along-shelf and cross-shelf momentum balances indicate three dynamically distinct regions: the surf zone, the inner shelf between the offshore edge of the surf zone and the 13-m isobath, and the midshelf extending offshore of the 13-m isobath (Figure 16). Consistent with previous studies, breaking surface gravity waves provide the dominant forcing in the surf zone. The cross-shelf divergence in the cross-shelf component of the wave radiation stress $\partial S_{xx}/\partial x$ is much larger than the other estimated terms, suggesting it is balanced by a cross-shelf pressure gradient (i.e., wave setup that could not be estimated with these data). The present estimates also support previous conclusions [*Thornton and Guza*, 1986; *Feddersen et al.*, 1998] that the cross-shelf divergence in the along-shelf component of the wave radiation stress $\partial S_{xy}/\partial x$ is largely balanced by bottom stress. This balance requires a linear drag coefficient for the subtidal flow in the surf zone that is about 10 times larger than the drag coefficient seaward of the surf zone.

The cross-shelf momentum balance at midshelf is predominantly geostrophic; that is, the Coriolis force due to the along-shelf current balances the cross-shelf pressure gradient, as found elsewhere [*Brown et al.*, 1985, 1987; *Lee et al.*, 1984, 1989]. At this site the along-shelf flow is geostrophic into fairly shallow water, the 21-m isobath. The along-shelf momentum balance at midshelf is more complex. The wind stress and the along-shelf pressure gradient terms are similar in magnitude and are balanced by both accelerations and bottom stress, consistent with previous studies [*Allen and Smith*, 1981; *Lentz and Winant*, 1986; *Lee et al.*, 1984, 1989; *Lentz*, 1994].

Between the surf zone and midshelf is a transition region referred to as the inner shelf, here extending roughly from the 4- to the 13-m isobath. The along-shelf momentum balance over the inner shelf is predominantly between wind and bottom stresses, consistent with the few previous studies of the momentum balance in 10 to 15 m of water [*Lentz and Winant*, 1986; *Lee et al.*, 1989]. Along-shelf pressure gradients were important over the inner shelf during a few events associated with a low-salinity plume from Chesapeake Bay, approximately 100 km north of the study site [*Rennie et al.*, this issue]. In the cross-shelf direction the Coriolis force due to the along-shelf current, $\partial S_{xx}/\partial x$ from the shoaling of unbroken surface gravity waves, and the cross-shelf pressure gradient all have similar magnitudes. The cross-shelf wind stress is never a dominant term. The cross-shelf wind stress is similar in magnitude to the Coriolis force at the 8-m site, consistent with the results of *Lee et al.* [1989] at 10-m water depth in the South Atlantic Bight. However, the radiation stress gradient $\partial S_{xx}/\partial x$, a term not considered by *Lee et al.* [1989], dominates at the 8-m site. Assuming the cross-shelf pressure gradient balances the other terms, the pressure gradient may be thought of as a superposition of a geostrophic along-shelf flow and wave setdown. The strongest along-shelf currents coincided with the largest surface waves, and geostrophic setup (southeastward flows) and wave setdown approximately cancelled in 13-m depth, resulting in a nearly flat mean sea surface during some events.

On both the inner and midshelf the depth-averaged, cross-shelf pressure gradient includes a baroclinic component (cross-shelf density gradient) that balances about one third to one half of the barotropic component (cross-shelf sea surface slope). This contrasts with results for winter in the South Atlantic Bight, where estimates of the baroclinic component (from shipboard CTD surveys) were small compared to the barotropic component [*Lee et al.*, 1984, 1989]. The baroclinic cross-shelf pressure gradient is in thermal wind balance with the vertical shear in the along-shelf flow in water as shallow as 10 m.

The depth-averaged, cross-shelf velocities are too small to estimate accurately from the observations, but the tendency for the along-shelf momentum balance to close without including the Coriolis force $f\bar{u}$ (Figure 8 and Plate 1) suggests $f\bar{u}$ is not a large term in the along-shelf momentum balance. Several previous studies have found similar results for the midshelf and inner shelf [*Allen and Smith*, 1981; *Lentz and Winant*, 1986; *Lee et al.*, 1989], though *Lee et al.* [1984, 1989] find $f\bar{u}$ is large over the outer shelf in the South Atlantic Bight. In general, the depth-averaged, cross-shelf flow remains poorly understood. If $f\bar{u}$ is small, the along-shelf and cross-shelf, depth-averaged momentum balances decouple and the along-shelf momentum balance in these three regions provides a simple estimate of the depth-averaged, along-shelf current in terms of the forcing, i.e., along-shelf wind and wave stresses and the along-shelf pressure gradient. This simple estimate reproduces accurately the observed depth-averaged, along-shelf current and its cross-shelf variation from the surf zone to midshelf, given a linear drag coefficient of 5×10^{-3} m s^{-1} within the surf zone and 5×10^{-4} m s^{-1} seaward of the surf zone.

Appendix

The procedure for estimating terms in the depth-averaged momentum balances (1) and (2) is described in section A1. Uncertainties in the estimates are discussed in section A2, and bottom stress estimates from the linear drag law are compared to log-profile estimates in section A3.

A1. Estimation of Terms

Terms in the momentum balances are estimated using the hourly data and then low-pass filtered (half-power point 38 hours) to focus on subtidal variability. Vertical integrals are estimated using a trapezoidal rule and assuming no vertical variations near the boundaries to extrapolate to the surface and bottom.

A1.1. Accelerations. Time derivatives are estimated as centered differences over 2-hour intervals.

A1.2. Pressure gradients. The depth-averaged pressure gradient in (1) and (2) is estimated from the bottom pressure and density data by substituting (4) into (3) or the equivalent equation for $\partial P/\partial y$. The density term in (3) is estimated more easily from the moored observations by noting that

$$\int_{-h}^{0} g \frac{\partial \rho}{\partial x}\left(1+\frac{z}{h}\right) dz = \frac{\partial}{\partial x}\int_{-h}^{0} \rho g \, dz + \frac{1}{h}\frac{\partial}{\partial x}\int_{-h}^{0} \rho g z \, dz. \tag{A1}$$

The integrals on the right-hand side are estimated for each mooring site where density estimates are available. The cross-shelf gradients of the bottom pressure and the density integrals are estimated as finite differences roughly centered on the site of interest. For example, the cross-shelf pressure gradient estimate for the 21-m site is the difference between bottom pressure and density estimates from the 26- and 5-m sites (bottom pressure at the 5-m site and density from the FRF pier site) divided by the separation. The 13-m estimate is from the 21- and 5-m sites, and the 26-m estimate is from the 33- and 5-m sites (Figure 2). Accurate cross-shelf pressure gradients can be made only for the 13-, 21-, and 26-m sites. The bottom pressure and density measurements at the 13- and 5-m sites were too close together (separation 1 km) to make reliable estimates of the depth-averaged pressure gradient. There are bottom pressure but no density measurements offshore of the 26-m site (Figure 2). Therefore the density gradient term in (3) for the 26-m site is estimated using observations from the 21- and 26-m sites.

Along-shelf pressure gradients are estimated along the 5- and 21-m isobaths using data from the along-shelf pressure/density array (Figure 1). Density along the 5-m isobath is assumed vertically uniform because temperature and conductivity were measured at only one depth. Pressure gradients along the 5-m isobath are estimated as differences between measurements from the sites 17 km north and south of the central line. Pressure gradients along the 21-m isobath are estimated as differences between measurements from the sites 32 km north and 27 km south of the central line. Pressure gradient estimates from different pairs of bottom pressure

sensors along either the 5- or 21-m isobaths yielded similar estimates. The pressure gradient estimate along the 5-m isobath is compared with the other terms in the along-shelf momentum balance from the 4-, 8-, and 13-m sites and the pressure gradient along the 21-m isobath to terms from the 21- and 26-m sites.

A1.3. Wind, bottom, and wave radiation stresses. The wind stress is estimated using a neutral drag law [*Large and Pond*, 1981] and the FRF pier winds. Other neutral and nonneutral bulk estimates [*Fairall et al.*, 1996] give nearly identical wind stresses [*Austin and Lentz*, this issue]. No attempt has been made to account for the influence of waves and the shallowness of the water in the drag law used because the dependence of the drag coefficients on these effects is not well understood [*Geernaert*, 1988]. The FRF pier winds are used because there is a continuous time series over the duration of the study and the pier wind measurements are nearly identical to the wind measurements at the 21-m site (magnitude of the vector correlation is 0.98).

Bottom stress is estimated assuming a linear drag law (5) with $r = 5 \times 10^{-4}$ m s^{-1}. This choice is motivated by simplicity and the poor understanding of the factors influencing bottom stress in the surf zone and inner shelf. Bottom stress estimates from (5) are compared with log-profile estimates using bottom tripod measurements at the 21-m site in Section A3.

Wave radiation stresses are estimated in 8-m depth from the FRF wave-directional array data and a directional moment estimation technique [*Elgar et al.*, 1994]. To estimate S_{xy} at other locations, the depth and surface wave properties are assumed not to vary in the along-shelf direction and the wave field is assumed narrow-banded in both frequency and direction. In this case [*Longuet-Higgins and Stewart*, 1964]

$$S_{xy} = Ec_g \sin(2\theta)/(2c) \tag{A2}$$

where $E = \rho_0 g H_{sig}^2/16$ is the wave energy, H_{sig} is the significant wave height, ρ_0 is a reference density, g is gravitational acceleration, and c_g and c are the (linear theory) group and phase velocities, respectively, at the peak wave frequency. The angle θ in 8-m depth is chosen such that S_{xy} from (A2) equals the measured S_{xy} in 8-m depth (using values of E, and of c and c_g based on the peak frequency, measured in 8-m depth) [*Thornton and Guza*, 1986].

The cross-shelf gradient in S_{xy} at each measurement site, using (A2) and Snell's law is given by

$$\frac{\partial S_{xy}}{\partial x} = \varepsilon \sin(\theta)/c \tag{A3}$$

where the wave dissipation $\varepsilon = \partial[Ec_g \cos(\theta)]/\partial x$ is estimated using the model of Whitford and Thornton [*Church and Thornton*, 1993], with $B = 0.72$ and $\gamma = 0.3$ [*Chen et al.*, 1997]. The modeled dissipation rate depends linearly on the local bottom slope (estimated from bathymetric surveys; see Figure 2) and on the local wave energy (obtained by applying linear theory to the bottom pressure spectrum at sea-swell frequencies measured near each mooring/tower.) Cross-shelf gradients of

$$S_{xx} = E\left\{\frac{c_g}{c}[1 + \cos^2(\theta)] - \frac{1}{2}\right\} \tag{A4}$$

were estimated similarly using estimates of dissipation from the model and estimates of E and the peak wave frequency from observations at each site. When there is no wave breaking, S_{xy} gradients vanish but S_{xx} gradients are nonzero (e.g., *Longuet-Higgins and Stewart* [1964] and (15)).

A2. Uncertainties

Uncertainties in the estimates described above cannot be quantified accurately because instrument performance in the field is not understood well and because spatial scales of variation are unknown. Nevertheless, a qualitative discussion of uncertainties provides some context for interpreting the estimates presented in section 3.

Errors in the depth-averaged velocity estimates include current speed and direction measurement errors and errors in estimating the depth-averaged currents from a few vertically spaced current measurements. The current meters have a reported accuracy of 2–3 cm s^{-1} [*Beardsley*, 1987; *Guza et al.*, 1988]. Uncertainties in orientation have a larger impact on the cross-shelf velocities than along-shelf velocities because the flows are strongly polarized (Table 1). The largest source of error in estimating depth averages is probably extrapolation of the current profiles to the surface and bottom. However, comparison of the standard estimate at the 21-m site with an estimate incorporating near-surface ocean surface current radar (OSCR) [*Shay et al.*, 1998] and near-bottom tripod (Section A3) current measurements yielded rms differences in depth-averaged velocities of 1 cm s^{-1}. Maximum differences were 5 cm s^{-1} for hourly data and 3 cm s^{-1} for low-pass-filtered data. This suggests depth averaging at this site does not increase substantially the uncertainty in the estimates over the uncertainty in the individual current measurements. Current meter uncertainties include wave-induced biases that may affect all instruments on a mooring, and thus it cannot be assumed that depth averaging will reduce the uncertainty from that for an individual current meter. Therefore $\delta u = 3$ cm s^{-1} is the assumed uncertainty in both the currents and the depth-averaged currents. The subtidal accelerations have an estimated uncertainty of $\delta u/\Delta t$, where a Δt of 9 hours was chosen as approximately a quarter of the 38-hour cutoff period for the low-pass filter (Table A1). Estimated uncertainty in the Coriolis terms is $f\delta u$.

Parallel plate pressure ports were added to the Seagauges to reduce flow noise. On the basis of flume tests (flow speeds of 6–40 cm s^{-1}) and ocean deployments of several sensors at the same site, the pressure measurements have a relative accuracy of 0.1–0.2 mbar. The influence of waves on the pressure measurements is not known. Comparisons of the Seagauges and Setra pressure sensors at the 5- and 21-m central line sites indicate relative accuracies between these pairs of ~1 mbar. Uncertainties in the bottom pressure gradient terms are $100(\delta P_b/\Delta x)/\rho_0$ (100 is the conversion from mbar to N m^{-2}), where δP_b is assumed to be 0.2 mbar for Seagauge pairs and 1 mbar for Seagauge-Setra pairs. Uncertainties in the density are estimated to be 0.1 kg m^{-3} based on comparisons with shipboard CTD measurements and between adjacent instruments on the same mooring when the water column is thought to be well mixed. Uncertainties arise primarily from drift of the conductivity cells [*Alessi et al.*, 1996]. Uncertainties in the depth-averaged densities due to having only two instruments at the northern and southern 21-m sites were estimated by comparing depth averages using all four instruments at the central 21-m site with estimates using only two instruments. The rms differences were 0.25 kg m^{-3}. Thus $\delta\rho$ is assumed to be 0.1 kg m^{-3}, except for the along-shelf gradient at the 21-m site, where

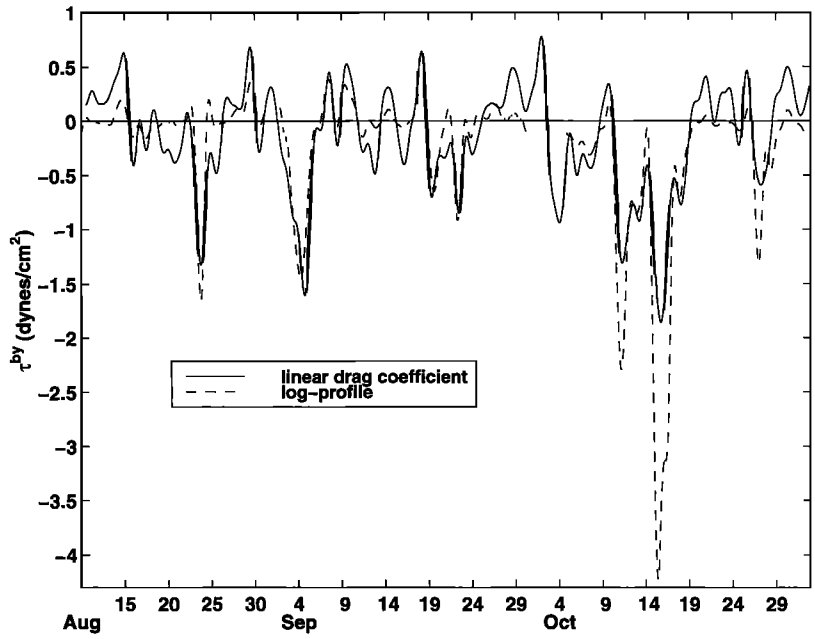

Figure A1. Time series of along-shelf bottom stress at the 21-m site estimated using a linear drag law with $r = 5 \times 10^{-4}$ m s^{-1} and log profiles from either a bottom tripod or a bottom tetrapod. Tetrapod-based estimates are shown during August, when a tripod and tetrapod were both deployed.

it is assumed to be 0.25 kg m^{-3}. Uncertainties in the baroclinic pressure gradient are estimated as $gh\delta\rho/(\rho_0\Delta x)$. There is additional uncertainty associated with cross-shelf variations in $\partial P/\partial y$ between 5 and 13 m and between 21 and 26 m because $\partial P/\partial y$ is estimated only along two isobaths.

Hourly wind stress estimates from the FRF pier and the 21-m site (separation ~5 km) have rms differences of 2–3 $\times$ 10^{-2} N m^{-2}. These differences are presumably from both instrument inaccuracies and spatial variations in the wind, which is assumed to be spatially uniform. Thus the estimated uncertainty is $\delta\tau^s/(\rho_0 h)$ with $\delta\tau^s = 3 \times 10^{-2}$ N m^{-2}. Another major source of uncertainty is the drag coefficient in shallow water and its dependence on sea state and wind direction (fetch). A summary of drag coefficient estimates in shallow water by *Geernaert* [1988] suggests uncertainties of about 20%. Recent evidence suggests the drag coefficient over the inner shelf may be different for onshore and offshore winds [*Friedrichs and Wright*, 1998].

Uncertainties in the bottom stress term owing to uncertainties in the current measurements are $r\delta u/h$. However, of more concern is the dependence of r on factors such as waves, bottom roughness, and stratification, and, more generally, the appropriateness of a linear drag law for parameterizing bottom stress. A comparison of the linear drag and log-profile estimates of bottom stress at the 21-m site is given in section A3.

The radiation stress gradient estimates are crude. Errors are due to uncertainties in the bottom slope, errors in linear theory, and errors in model-based estimates of the breaking wave dissipation rate. The radiation stress gradient estimates for nonbreaking waves are probably accurate within 50% but may be less accurate for breaking waves. When the fraction of waves breaking is low, but not negligible, as occurs in the region bordering the seaward edge of the surf zone, the true S_{xx} gradient changes sign and the estimates may have larger fractional errors and/or the wrong sign.

A3. Bottom Stress Estimates

The linear drag formulation used to estimate bottom stress is crude because it does not account for factors such as variability in bottom roughness and surface gravity waves. Bottom tripod and tetrapod [*Kim et al.*, 1997] deployments at the 21-m site provide independent bottom stress estimates.

The 1-m-tall tetrapods supported four Marsh-McBirney electromagnetic current meters sampling at 1 Hz for 1024 s every 4 hours and an altimeter that determined the sensor elevations above the seafloor. There were 30-day tetrapod deployments during August and October. The 5-m-tall bottom tripods supported five benthic acoustic stress sensor (BASS) current meters [*Williams et al.*, 1987] and seven thermistors. Currents were sampled nearly continuously at approximately 1.5 Hz. There were 30-day tripod deployments during July–August and September. There is generally good agreement between the nearest-bottom vector-measuring current meter (VMCM) (elevation 1.5 m) on the 21-m mooring and the BASS tripod and electromagnetic current meter (EMCM) tet-

Table A1. Estimated Uncertainties in Terms of Cross-Shelf and Along-Shelf Momentum Balances, Equations (1) and (2)

Term	Site				
	4 m	8 m	13 m	21 m	26 m
$\delta u/\Delta t$	0.1	0.1	0.1	0.1	0.1
$f\delta u$	0.3	0.3	0.3	0.3	0.3
$\delta P_b(\rho_0\Delta x)$	···	11.7	0.4	0.7	0.3
$gh\delta\rho/(\rho_0\Delta x)$	···	0.9	0.3	0.1	0.1
$\delta P_b/(\rho_0\Delta y)$	0.06	···	···	0.03	···
$gh\delta\rho/(\rho_0\Delta y)$	0.02	···	···	0.08	···
$\delta\tau^s/(\rho_0 h)$	0.7	0.4	0.2	0.1	0.1
$\delta\tau^b/(\rho_0 h)$	0.4	0.2	0.1	0.1	0.1

Units are 10^{-5} m s^{-2}.

Table A2. Correlations Between Subtidal Bottom Stresses τ^b Estimated at the 21-m Site From a Linear Drag Law (Using Mooring Observations) and Log Profiles (Using Tripod and Tetrapod Observations)

Deployment	Filtered τ^{by}	Filtered τ^{bx}	Duration, days	Current Meter Elevation, m
Full time series	0.81*	0.45*	74	
Aug. tetrapod	0.79*	0.39	20	0.06, 0.35, 0.66, 0.95
Oct. tetrapod	0.87*	0.56	28	0.05, 0.34, 0.65, 0.94
Aug. tripod	0.94*	0.75	12	0.24, 1.20, 2.55, 4.44
Sept. tripod	0.89*	0.52	26	0.24, 0.60, 1.20, 2.55, 4.44

Duration refers to measurements used in the correlations.
*Correlations are significantly different from zero at the 95% confidence level.

rapod current measurements, with the exception of the October tetrapod deployment, when along-shelf tetrapod velocities exceeded the VMCM velocities, despite being closer to the bottom. It is unclear which measurements are correct.

Bottom stresses are estimated from the tripod and tetrapod data using a log-profile technique [e.g., *Kim et al.*, 1997]. Only the two sensors closest to the seafloor are used to estimate bottom stress, as there is curvature in the speed profiles, perhaps because the water column is often stratified within a few meters of the bottom. Using the lowest three, rather than the lowest two sensors, has little effect on the bottom stress estimates, except during October, when the profile curvature is persistent and strong.

The along-shelf bottom stress estimates from log profiles and the linear drag law agree well (Figure A1). Zero-lag correlations are 0.79 or greater for each tripod/tetrapod deployment and for the combined time series (Table A2). The most notable discrepancies are the three events in October, when the log-profile estimates yield bottom stresses that are about twice as large as the linear drag law (Figure A1). It is unclear which estimate is more accurate. If log-profile estimates of bottom stress are used instead of linear drag law estimates, the correlation between forcing and flow response at the 21-m site is slightly (though not significantly) increased, from 0.88 (Table 3) to 0.91. Correlations between linear and log-profile bottom stress estimates are smaller for the weaker cross-shelf component of bottom stress (Table A2), but the magnitudes of both estimates are similar and much smaller than other terms in the cross-shelf momentum balance (Table 4). As log-profile estimates are available only at the 21-m site, the linear drag law is used at all sites.

Acknowledgements. Pier end wind and 8-m wave observations were acquired by staff at the Field Research Facility of the U.S. Army Corps of Engineers Waterways Experiment Stations's Coastal Engineering Research Center. Permission to use these data is greatly appreciated. Thanks to B. Raubenheimer and E. Gallagher for help collecting the 4- and 8-m tower data. Financial support was provided by the Ocean Sciences Division of the National Science Foundation (Coastal Ocean Processes program) and by the Office of Naval Research (Coastal Dynamics and AASERT programs).

References

Alessi, C. A., S. J. Lentz, and J. Austin, Coastal Ocean Processes Inner-Shelf Study: Coastal and moored physical oceanographic measurements, *Tech. Rep. WHOI-96-06*, 142 pp., Woods Hole Oceanogr. Inst., Woods Hole, Mass., 1996.

Allen, J. S., and R. L. Smith, On the dynamics of wind-driven shelf currents, *Philos. Trans. R. Soc. London, Ser. A*, *302*, 617–634, 1981.

Austin, J. A., and S. J. Lentz, The relationship between synoptic weather systems and meteorological forcing on the North Carolina inner shelf, *J. Geophys. Res.*, this issue.

Battjes, J. A., and M. J. F. Stive, Calibration and verification of a dissipation model for random breaking waves, *J. Geophys. Res.*, *90*, 9159–9167, 1985.

Beardsley, R. C., A comparison of the vector-averaging current meter and new Edgerton, Germeshausen, and Grier, Inc., vector-measuring current meter on a surface mooring in CODE 1, *J. Geophys. Res.*, *92*, 1845–1860, 1987.

Boicourt, W. C., The circulation of water on the continental shelf from Chesapeake Bay to Cape Hatteras, Ph.D. thesis, 183 pp., Johns Hopkins Univ., Baltimore, Md., 1973.

Bowen, A. J., D. L. Inman, and V. P. Simmons, Wave "set-down" and set-up, *J. Geophys. Res.*, *73*, 2569–2577, 1968.

Brown, W. S., N. R. Pettigrew, and J. D. Irish, The Nantucket Shoals Flux Experiment (NSFE79), II, The structure and variability of across-shelf pressure gradients, *J. Phys. Oceanogr.*, *15*, 749–771, 1985.

Brown, W. S., J. D. Irish, and C. D. Winant, A description of subtidal pressure field observations on the northern California shelf during the Coastal Ocean Dynamics Experiment, *J. Geophys. Res.*, *92*, 1605–1636, 1987.

Butman, C. A., CoOP: Coastal Ocean Processes Study—Interdisciplinary approach, new technology to determine coupled biological, physical, geological processes affecting larval transport on inner shelf, *Sea Technol.*, *35*, 44–49, 1994.

Chen, Y., R. T. Guza, and S. Elgar, Modeling spectra of breaking surface waves in shallow water, *J. Geophys. Res.*, *102*, 25,035–25,046, 1997.

Church, J. C., and E. B. Thornton, Effects of breaking wave induced turbulence within a longshore current model, *Coastal Eng.*, *20*, 1–28, 1993.

Elgar, S., T. H. C. Herbers, and R. T. Guza, Reflection of ocean surface gravity waves from a natural beach, *J. Phys. Oceanogr.*, *24*, 1503–1511, 1994.

Fairall, C. W., E. F. Bradley, D. P. Rogers, J. B. Edson, and G. S. Young, Bulk parameterization of air-sea fluxes for Tropical Ocean-Global Atmosphere Coupled-Ocean Atmosphere Response Experiment, *J. Geophys. Res.*, *101*, 3747–3764, 1996.

Feddersen, F., R. T. Guza, S. Elgar, and T. H. C. Herbers, Longshore momentum balances in the nearshore, *J. Geophys. Res.*, *103*, 15,667–15,676, 1998.

Fofonoff, N. P., and R. C. Millard Jr., Algorithms for computation of fundamental properties of seawater, *UNESCO Tech. Pap. Mar. Sci.*, *44*, 53 pp., 1983.

Friedrichs, C. T., and L. D. Wright, Wave effects on inner shelf wind drag coefficients, in *Ocean Wave Measurement and Analysis: Proceedings of the 3rd International Symposium on Ocean Wave Measurement and Analysis*, edited by B. Edge and J. Hemsley, pp. 1033–1047, Am. Soc. of Civ. Eng., New York, 1998.

Garcez-Faria, A. F., E. B. Thornton, T. P. Stanton, C. V. Soares, and T. C. Lippman, Vertical profiles of longshore currents and related bed shear stress and bottom roughness, *J. Geophys. Res.*, *103*, 3217–3232, 1998.

Geernaert, G., Drag coefficient modeling for the near coastal zone, *Dyn. Atmos. Oceans*, *11*, 307–322, 1988.

Guza, R. T., M. C. Clifton, and F. Rezvani, Field intercomparisons of electromagnetic current meters, *J. Geophys. Res.*, *93*, 9302–9314, 1988.

Kim, S. C., L. D. Wright, and B. O. Kim, The combined effects of synoptic-scale and local-scale meteorological events on bed stress and sediment transport on the inner shelf of the Middle Atlantic Bight, *Cont. Shelf Res.*, *17*, 407–433, 1997.

Large, W. G., and S. Pond, Open ocean momentum flux measurements in moderate to strong winds, *J. Phys. Oceanogr.*, *11*, 324–336, 1981.

Lee, T. N., W. J. Ho, V. Kourafalou, and J. D. Wang, Circulation on the continental shelf of the Southeastern United States, I, Subtidal response to wind and Gulf Stream forcing during winter, *J. Phys. Oceanogr.*, *14*, 1001–1012, 1984.

Lee, T. N., E. Williams, R. E. J. Wang, and L. Atkinson, Response of South Carolina continental shelf waters to wind and Gulf Stream forcing during winter of 1986, *J. Geophys. Res.*, *94*, 10,715–10,754, 1989.

Lentz, S. J., Current dynamics over the northern California inner shelf, *J. Phys. Oceanogr.*, *24*, 2461–2478, 1994.

Lentz, S. J., and C. D. Winant, Subinertial currents on the southern California shelf, *J. Phys. Oceanogr.*, *16*, 1737–1750, 1986.

Long, C. E., Index and bulk parameters for frequency-distribution spectra measured at CERC Field Research Facility, June 1994 to August 1995, *Tech. Rep. Misc. Pap. CERC-96-6*, U.S. Army Eng. Waterw. Exp. Stn., Vicksburg, Miss., 1996.

Longuet-Higgins, M. S., and R. W. Stewart, Radiation stresses in water waves; A physical discussion, with applications, *Deep Sea Res.*, *11*, 529–562, 1964.

Masse, A. K., Estuary-shelf interaction: Delaware Bay and the inner shelf, Ph.D. thesis, 216 pp., Univ. of Del., Newark, 1988.

Noble, M., and B. Butman, Low-frequency wind-induced sea level oscillations along the east coast of North America, *J. Geophys. Res.*, *84*, 3227–3236, 1979.

Pettigrew, N. R., The dynamics and kinematics of the coastal boundary layer off Long Island, Ph.D. thesis, 262 pp., Woods Hole Oceanogr. Inst., Woods Hole, Mass., 1981.

Rennie, S. E., J. L. Largier, and S. J. Lentz, Observations of a pulsed buoyancy current downstream of Chesapeake Bay, *J. Geophys. Res.*, this issue.

Scott, J. T., and G. T. Csanady, Nearshore currents off Long Island, *J. Geophys. Res.*, *81*, 5401–5409, 1976.

Shay, L. K., S. J. Lentz, H. C. Graber, and B. K. Haus, Current structure variations detected by high frequency radar and vector measuring current meters, *J. Atmos. Oceanic Technol.*, *15*, 237–256, 1998.

Svendsen, I. A., and U. Putrevu, Nearshore mixing and dispersion, *Proc. R. Soc. London, Ser. A*, *445*, 561–576, 1994.

Thornton, E. B., and R. T. Guza, Transformation of wave height distribution, *J. Geophys. Res.*, *88*, 5925–5938, 1984.

Thornton, E. B., and R. T. Guza, Surf zone longshore currents and random waves: Field data and models, *J. Phys. Oceanogr.*, *16*, 1165–1178, 1986.

Waldorf, B. W., J. L. Largier, S. Rennie, J. Austin, and C. Greengrove, Coastal Ocean Processes (CoOP) pilot project data report: R/V *Cape Hatteras* shipboard measurements; underway, CTD, and ADCP data August 1994, *Tech. Rep. SIO Ref. Ser. 95-29*, 419 pp., Scripps Inst. of Oceanogr., La Jolla, Calif., 1995.

Waldorf, B. W., J. L. Largier, S. Rennie, and J. Austin, Coastal Ocean Processes (CoOP) pilot project data report: R/V *Cape Hatteras* shipboard measurements; underway, CTD, and ADCP data October 1994, *Tech. Rep. SIO Ref. Ser. 96-9*, 407 pp., Scripps Inst. of Oceanogr., La Jolla, Calif., 1996.

Wang, D. P., Low frequency sea level variability on the Middle Atlantic Bight, *J. Mar. Res.*, *37*, 683–697, 1979.

Whitford, D. J., and E. B. Thornton, Comparison of wind and wave forcing of longshore currents, *Cont. Shelf Res.*, *13*, 1205–1218, 1993.

Williams, A. J., J. S. Tochko, R. L. Koehler, W. D. Grant, T. F. Gross, and C. V. R. Dunn, Measurement of turbulence in the oceanic bottom boundary layer with an acoustic current meter array, *J. Atmos. Oceanic Technol.*, *4*, 312–327, 1987.

Winant, C., R. Beardsley, and R. Davis, Moored wind, temperature and current observations made during CODE-1 and CODE-2 over the northern California continental shelf and upper slope, *J. Geophys. Res.*, *92*, 1569–1604, 1987.

Yankovsky, A. E., and R. W. Garvine, Subinertial dynamics on the inner New Jersey shelf during the upwelling season, *J. Phys. Oceanogr.*, *28*, 2444–2458, 1998.

S. Elgar, School of Electrical Engineering and Computer Science, Washington State University, Pullman, WA 99164.

F. Feddersen and R. T. Guza, Center for Coastal Studies, Scripps Institution of Oceanography, University of California, San Diego, La Jolla, CA 92093.

T. H. C. Herbers, Department of Oceanography, Naval Postgraduate School, Code OC/He, Monterey, CA 93943.

S. Lentz, Woods Hole Oceanographic Institution, MS 21, Woods Hole, MA 02543. (slentz@whoi.edu)

(Received August 5, 1998; revised January 27, 1999;
accepted February 24, 1999.)